iScience

CellPress

Article

Template-free Synthesis of Stable Cobalt Manganese Spinel Hollow Nanostructured Catalysts for Highly Water-Resistant CO Oxidation

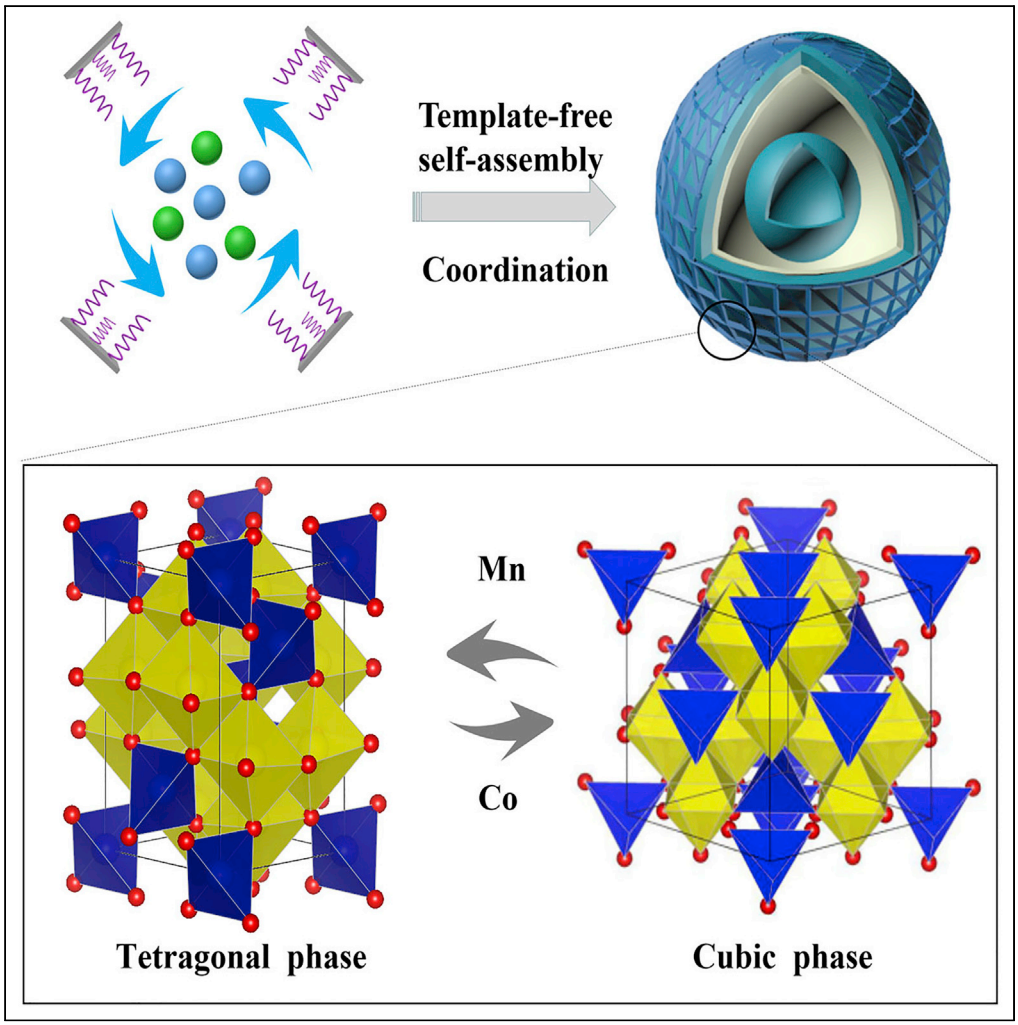

Zehai Xu, Yufan Zhang, Xiong Li, ..., Qingbiao Li, Baohua Mao, Zhi Liu

guoliangz@zjut.edu.cn (G.Z.)
kelqb@xmu.edu.cn (Q.L.)

HIGHLIGHTS

Multi-shell mesoporous spinel nanostructure was first designed by template-free method

$Co_xMn_yO_4$ catalyst configured by 16-nm spinel nanosheets held unique surface chemistry

Oxygen vacancy can be adjusted by controlling crystal phase and plane lattice parameter

The water-resisting $Co_xMn_yO_4$ spinel catalyst represents a benchmark in CO oxidation

Xu et al., iScience *21*, 19–30
November 22, 2019
https://doi.org/10.1016/j.isci.2019.10.013

iScience

CellPress

Article

Template-free Synthesis of Stable Cobalt Manganese Spinel Hollow Nanostructured Catalysts for Highly Water-Resistant CO Oxidation

Zehai Xu,[1,8] Yufan Zhang,[2,8] Xiong Li,[1] Lei Qin,[1] Qin Meng,[3] Guoliang Zhang,[1,5,9,*] Zheng Fan,[1] Zhen Xue,[1] Xinwen Guo,[4] Qinglin Liu,[5] Qingbiao Li,[5,6,*] Baohua Mao,[7] and Zhi Liu[7]

SUMMARY

Development of spinel oxides as low-cost and high-efficiency catalysts is highly desirable; however, rational synthesis of efficient and stable spinel systems with precisely controlled structure and components remains challenging. We demonstrate the design of complex nanostructured cobalt-based bimetallic spinel catalysts for low-temperature CO oxidation by a simple template-free method. The self-assembled multi-shelled mesoporous spinel nanostructures provide high surface area (203.5 m^2/g) and favorable unique surface chemistry for producing abundant active sites and lead to the creation of robust microsphere configured by 16-nm spinel nanosheets, which achieve satisfactory water-resisting property and catalytic activity. Theoretical models show that O vacancies at exposed {110} facets in cubic spinel phase guarantee the strong adsorption of reactive oxygen species on the surface of catalysts and play a key role in the prevention of deactivation under moisture-rich conditions. The design concept with architecture and composition control can be extended to other mixed transition metal oxide compositions.

INTRODUCTION

Transition metal and mixed transition metal oxides are among the immensely important compounds in the world and have offered significant application values in extensive fields like catalysis, energy storage, electronics, sensors, and magnetism (Poizot et al., 2000; de la Cruz et al., 2008; Wu et al., 2018). As one of the most intriguing groups of reducible transition metal oxides, which contain trivalent and bivalent cations in the lattice structure, spinel oxides exhibit more plentiful and complex surface compositions and structures than other materials (Bragg, 1915; Zhao et al., 2017; Xie et al., 2009). The morphology-dependent exposed crystal planes determine not only the surface geometric structure but also the surface composition and strongly affect the catalytic properties (Cargnello et al., 2013; Hu et al., 2008). Moreover, the concentration variation of the surface defects closely related to the crystal structure can significantly affect the catalytic activity in various catalytic processes (Huang, 2016). Compared with their monometallic analogs, bimetallic spinel oxide systems are superior in geometry and electronic characteristics, so that bimetallic systems can be designed as ordered mesoporous materials and possess distinctive chemical activities (Yu et al., 2017). Traditionally, the spinel compounds are generally synthesized by a solid-state method, which requires harsh conditions including elevated temperature, complicated procedures, and prolonged time to overcome reaction energy barriers. The produced spinels thus reveal large particle size, low surface area, and irregular shape, which might severely deteriorate their physicochemical properties (Wiley and Kaner, 1992; Lu et al., 2014). For decades many efforts have been made and some alternative moderate synthetic routes like sol-gel, solvothermal, and co-precipitation approaches have been developed (Lavela et al., 2007; Indra et al., 2014; Li et al., 2009). However, although spinel nanoparticles with metastable phases and tunable size can be obtained to some extent, the mild and rational synthesis of efficient and stable bimetallic spinel systems, especially with precise control over the lattice structures, chemical compositions, and morphologies of individual nanocrystals, still remains a big challenge.

The catalytic oxidation of combustion pollutants like carbon monoxide (CO) has drawn great attention, not only because of the relevance in vast industrial applications but also due to the importance as a key model reaction for grasping the mechanisms of catalysis (Xie et al., 2009; Cargnello et al., 2012; Christopher et al., 2011; Nie et al., 2017; Zhang et al., 2018; Saavedra et al., 2018). Noble metals function as high-performance catalysts in oxidation reactions, and the reaction temperature to complete oxidation can be sharply

[1]Institute of Oceanic and Environmental Chemical Engineering, State Key Lab Breeding Base of Green Chemical Synthesis Technology, Zhejiang University of Technology, Hangzhou 310014, P. R. China

[2]Department of Mechanical Engineering, College of Engineering, Carnegie Mellon University, Pittsburgh, PA 15213, USA

[3]College of Chemical and Biological Engineering, State Key Laboratory of Chemical Engineering, Zhejiang University, Hangzhou 310027, P. R. China

[4]State Key Laboratory of Fine Chemicals, Department of Catalysis Chemistry and Engineering, Dalian University of Technology, Dalian 116012, P. R. China

[5]College of Chemistry and Chemical Engineering, National Laboratory for Green Chemical Productions of Alcohols, Ethers and Esters, Xiamen University, Xiamen, 361005, P. R. China

[6]Fujian Province Key Laboratory of Energy Cleaning Utilization and Development, Jimei University, Xiamen 361021, P. R. China

[7]Shanghai Institute of Microsystem and Information Technology, Chinese Academy of Sciences, Shanghai 200050, China

[8]These authors contributed equally

[9]Lead Contact

*Correspondence: guoliangz@zjut.edu.cn (G.Z.), kelqb@xmu.edu.cn (Q.L.)

https://doi.org/10.1016/j.isci.2019.10.013

reduced. However, the high cost and the scarcity of noble metals usually makes the produced catalysts less desirable (Song et al., 2014). Instead, spinel-type metal oxides free of noble metals are being urgently developed as high-performance and cost-efficient catalysts, technologically and pragmatically (Chen et al., 2011; Li et al., 2015a). Co_3O_4 proves to be one of the most active nonprecious spinel-type catalysts for low-temperature CO oxidation (Xie et al., 2009; Song et al., 2014). The cobalt-based occupancies such as $(CoM)_3O_4$ (M = Fe, Cu, Cr) are interesting bimetallic spinel oxide systems, which display specific influence of charge and coordinating state of cobalt on catalysis (Gu et al., 2015). Recently, attempts have also been made to put nanostructured Co_3O_4 on proper substrates like graphene to form bifunctional oxygen-involving electrocatalysts (Li et al., 2016a), but the structure collapsing and fast performance decay problems are usually caused by relatively simple architecture and weak interfacial interactions of the components, which result in irreversible deactivation during catalytic process. Moreover, although spinel oxides can deliver competitive catalytic performances compared with noble metal catalysts, the water poisoning problem generally faced by metal oxides and supported metal catalysts (including noble metals) developed for low-temperature CO oxidation greatly limited their practical application (Xie et al., 2009; Song et al., 2014). Even if the surface hydrophobicity modification realized by utilizing polymers emerges as a promising strategy to prevent deactivation of catalysts in the presence of water, the catalytic activity of these catalysts might be easily reduced due to the blockage of active sites and surface area caused by hydrophobic coatings (Chen et al., 2010; Kuo et al., 2014). Therefore, it is of paramount importance in the development of high-efficiency and stable non-precious catalytic systems for low-temperature CO oxidation reaction.

To prepare high-performance catalysts with resistance to deactivity and deformation for target reactions under harsh environment, the understanding of morphology complexity and surface structure would be crucial to uncover the atomic-scale characteristics. The hollow micro- or nanostructures with controllable size, shape, composition, and interior architecture have important implications in vast fields (Hu et al., 2011; Li and Shi, 2014; Dai et al., 2015; Li et al., 2016b). Encouraged by the observation on building novel 3D nanostructures such as foams and urchins to overcome the structure collapsing problems (Lu and Zhao, 2015; You et al., 2016), we go forward to think that it a feasible strategy to design spinel oxide systems on the basis of forming robust multi-shelled hollow microsphere structure to enhance the catalytic activity and stability during long-term oxidation process. Meanwhile, largely due to the water strongly binding to metal-oxygen sites, monometallic catalysts often suffer severely from water poisoning at low temperature (Goodman et al., 2017). We also deem it necessary to explore suitable bimetallic systems to sharply improve the catalytic activity and minimize deactivation in the presence of steam. In this regard, the highly exposed active sites on the multi-shelled hollow nanostructures greatly improve the physicochemical characteristics and the formed robust hollow structure can prevent the possibility of collapsing during catalytic reactions. In addition, the synergistic and coordinative effects of metal oxides' self-support interface from bimetallic spinels may be maximized, which is critical in catalytic performance.

Herein, we report the preparation of hierarchical multi-shelled hollow microsphere mesoporous nanocatalysts from cobalt-based bimetallic spinels, which are long-term stable in the presence of steam. By tuning the structure and composition in a facile manner, we carried out CO oxidation to explore the catalytic activities and stabilities of different series of cobalt-based spinel hollow microsphere nanocatalysts. The self-assembled multi-shelled hollow nanostructured catalysts were prepared in two steps (Figure 1): (1) synthesis of glycerine Co-based bimetallic nanostructures with different secondary units via a solvothermal approach that involves facile solution-based ion redistribution and coordination processes and (2) slow heating process induced by the crystallization of spinel phase and formation of cobalt-based spinel multi-shelled hollow microspheres at mild condition. The ultimate goal of this work was a simple and facile template-free method to design complex nanostructured bimetallic spinel catalysts for low-temperature CO oxidation. The robust bimetallic spinel microspheres consisted of bistratal mesoporous shells with large surface area, wide tunable size range, and abundant oxygen vacancies. The reagent molecules can easily enter the interior of hollow microspheres through the mesopores within cobalt-based bimetallic spinel shells, and the product can exit back out through these mesopores. Significantly, the outstanding water-resisting property enabled the study of synergistic effects and particle agglomeration behavior during the spinel-catalyzed CO oxidation in the presence of steam. The high chemical stability, as well as uniform mesoporous hierarchical multi-shelled structure with rich morphologies, suggests that the cobalt-based bimetallic spinel multi-shell hollow microspheres are an excellent spinel system for catalytic oxidation reactions at low temperature.

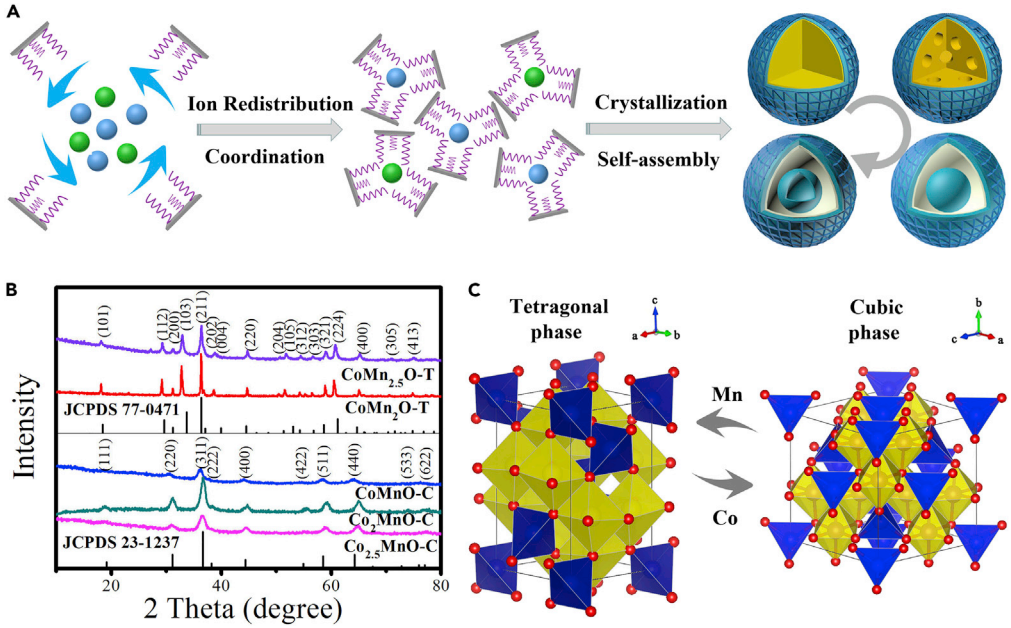

Figure 1. Scheme for Template-free Synthesis of Different Kinds of $Co_xMn_yO_4$ Mesoporous Nanostructured Materials

(A) The synthesis of $Co_xMn_yO_4$ spinel multi-shell hollow microspheres. Blue sphere: Co, green sphere: Mn, chain: glycerol.

(B) XRD patterns of as-prepared $Co_xMn_yO_4$ spinel with tetragonal and cubic phases. See also Figure S2.

(C) Transformation procedure in tetragonal and cubic phase $Co_xMn_yO_4$ spinel.

See also Figure S4.

RESULTS AND DISCUSSION

Among different varieties of mixed valence spinel oxides, manganese-based compounds have been proposed as a sort of interesting materials with versatile applications in view of their high abundance, low price, low toxicity, and environment friendliness. The physicochemical properties of $Co_xMn_yO_4$ spinels are highly sensitive to crystal phase and chemical composition, which greatly depend on the synthetic conditions (Chen et al., 2011; Li et al., 2015a). Tetragonal and cubic-phase $Co_xMn_yO_4$ spinels were first synthesized by tuning Co/Mn molar ratio in a wide range of 0.4–2.5, and the as-prepared spinel samples with different compositions were labeled as $CoMn_{2.5}O$-T, $CoMn_2O$-T, CoMnO-C, Co_2MnO-C, and $Co_{2.5}MnO$-C. After increasing the concentration of cobalt in microspheres, the crystal phase transformed from tetragonal to cubic phase (Figure 1C), which was confirmed by the color change of solution after solvothermal treatment (Figure S1). The corresponding X-ray diffraction (XRD) patterns (Figure 1B) display the Mn-rich samples with tetragonal phase (space group I41/amd (141)) and Co-rich hierarchical microspheres with cubic phase (space group Fd-3m (227)) (Menezes et al., 2015). In the fabrication of tetragonal $Co_xMn_yO_4$ spinels, no intermediate was found during the synthesis process (Figure S2A). The preferred orientation can be deduced from the intensity ratio of different facets. As depicted in Figure 1B, the intensity ratio of (112)/(211) was 0.43. The value of intensity ratio of (112)/(211) is larger than that of the standard (0.35) (JCPDS 77-0471), implying that the preferential orientation of $CoMn_{2.5}O$-T is [112] direction. As for $CoMn_2O$-T sample, the values of intensity ratios of (101)/(211) and (103)/(211) are 0.28 and 0.69, which are both greater than the standard, indicating that the b-axis orientation along the {010} plane is preferred. On the other hand, Mn ions in CoMn-glycerine complex were gradually oxidized to cubic Mn_7O_{13} in Co-rich environment; the formation of cubic cobalt manganese spinels was attributed to the cubic crystal structure and high Mn valence of intermediate Mn_7O_{13} (Figure S2B). The intensity ratios of (220)/(311) and (222)/(311) are 0.46 and 0.15 for cubic Co_2MnO-C spinels, respectively, which are also greater than the standard (JCPDS 23-1237). This change indicates the crystal of Co_2MnO-C orientated in the $[\bar{1}10]$ or $[1\bar{1}0]$ direction. Energy-dispersive X-ray spectroscopy and elemental analysis from X-ray photoelectron spectroscopy (XPS) prove the average atomic ratio of Co and Mn in as-prepared spinel compounds. Unlike cubic cobalt manganese spinels made by traditional solid-state methods, whose crystals are not stable at low temperature and easily transform into the tetragonal phase in

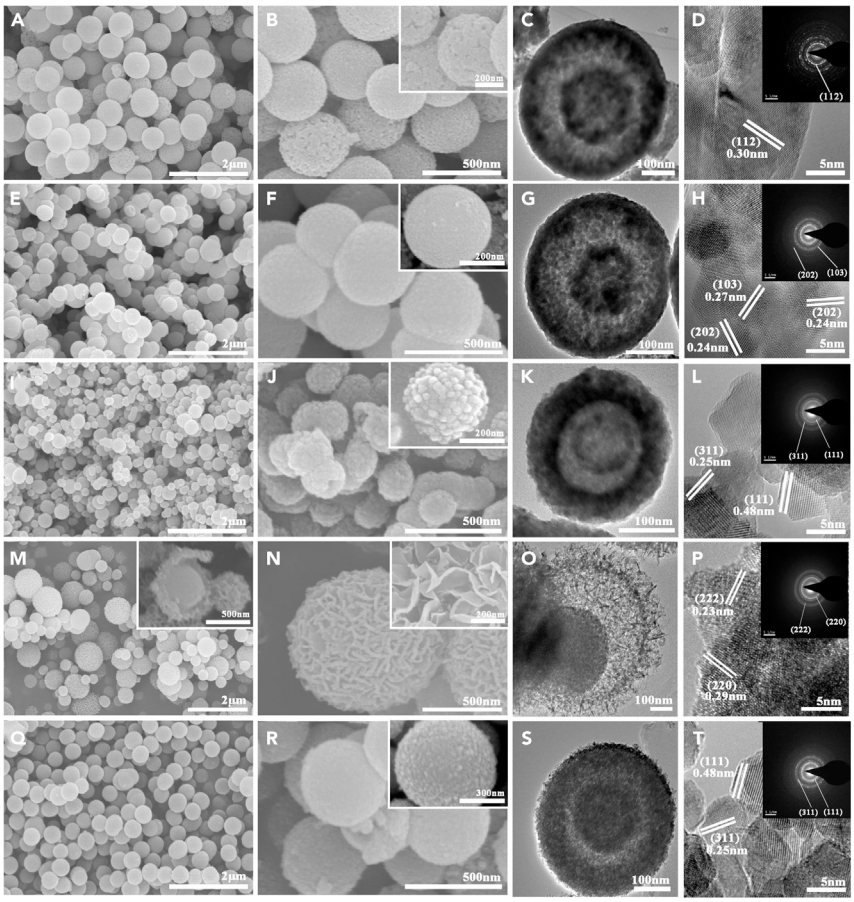

Figure 2. As-prepared $Co_xMn_yO_4$ Spinel Multi-Shell Hollow Microspheres Constructed by Different Building Blocks

(A–T) Scanning electron microscopic images of $CoMn_{2.5}O$-T (A and B), $CoMn_2O$-T (E and F), CoMnO-C (I and J), Co_2MnO-C (M and N), and $Co_{2.5}MnO$-C (Q and R) spinel microspheres. The mechanically broken hollow structure showing the internal cavities (inset in M) and 2D nanosheets as secondary unit constructed the flower-like hollow spheres (inset in N). See also Figure S3. TEM and HRTEM images of $CoMn_{2.5}O$-T (C and D), $CoMn_2O$-T (G and H), CoMnO-C (K and L), Co_2MnO-C (O and P), and $Co_{2.5}MnO$-C (S and T) spinel microspheres. The inset images are the corresponding fast Fourier transform patterns.

quenching process (Vila and Rojas, 1996), the as-prepared cubic $Co_xMn_yO_4$ spinels in this strategy are very stable, even at 0°C.

Controlled Morphology and Structure by Phase and Composition Adjustment

The morphological properties of as-prepared $Co_xMn_yO_4$ spinel hierarchical hollow microspheres were analyzed to confirm the structure controllability of catalysts, which strongly affects the physicochemical properties (Zhang and Lou, 2014). As observed in Figures 2 and S3, the shape, size, and interior structure of these microspheres were largely influenced by tuning the phase and composition. When the Co/Mn ratio was set as 0.4, dented $CoMn_{2.5}O$-T microspheres with close double shells of 80 nm interdistance and 500–700 nm diameter were produced (Figures 2A and 2B). The nanoparticles as secondary units stacked loosely on the surface to form a thin shell, which may be attributed to the low stacking fault energy under Mn-rich environment. After enhancing the Co/Mn ratio to 0.5, smooth $CoMn_2O$-T microspheres with a diameter of 400 nm and similar interdistances between the adjacent shells could be observed (Figures 2E and 2F). To further illustrate the configurations of hollow microspheres, transmission electron microscopic (TEM) and high-resolution TEM (HRTEM) analysis were employed to explore more details concerning the crystal structure of samples. The dominant exposed plane of $CoMn_{2.5}O$-T sample is {112}, which only exhibits a lattice distance of 0.30 nm (Figure 2D). Similarly, $CoMn_2O$-T spheres are observed to be disintegrated into a mass

of small nanocrystals with clear lattice fringes of 0.24 nm, and 0.27 nm corresponds to (202) and (103) crystal facets of $Co_xMn_yO_4$with tetragonal phase spinel structure (JCPDS 77-0471) (Chen et al., 2011; Li et al., 2015a), demonstrating that the exposure facet is mostly {010} (Figure 2H). When the Co/Mn ratio reached 1.0, glycerine-CoMn outer shell shrank more slowly and converted into cobalt manganese spinel shell. Compared with $Co_xMn_yO_4$-T samples, the thickness of shell for $Co_xMn_yO_4$-C microsphere increased to two times (Figure 2K). Interestingly, for flower-like Co_2MnO-C hollow microspheres (Figures 2M and 2N), the generated thin radially standing nanoflakes (16 nm) acted as 2D secondary building blocks and constructed highly rough outer shell due to the minimization of their surface energies by an oriented attachment. After elevating the content of cobalt, it was found that the nanoparticles were orderly arranged to form smooth surface again. The contraction effect was minimized, and the thickness of inner shell was enlarged as well as the outer shell, resulting in a minimum interdistance of ~20 nm between shells (Figures 2S and S4). Moreover, the exposed crystal facets of $Co_xMn_yO_4$ spinel microspheres changed, whereas the crystal phase transformed from tetragonal to cubic phase. According to the results of measured lattice distance in HRTEM images, the exposure facets of CoMnO-C, Co_2MnO-C, and $Co_{2.5}$MnO-C samples are mostly {112}, {110}, and {112}, respectively. These different reactive crystal facets in the selective synthesis of spinel nanomaterials play an important role in the formation of physicochemical characteristics of catalysts, indicating the highly active nature of the cobalt manganese spinel shell (Xie et al., 2009; Chen et al., 2011; Li et al., 2016c).

For nanosized materials to be catalytically active, a high-energy interfacial structure is of great significance. In previous examples of nanostructured spinel catalysts, transition metal oxides were often deposited on suitable supporting materials to obtain high-performance oxidation catalysts with structured stability (Ren et al., 2014; Liang et al., 2011). The weak interfacial interaction between different components thus might cause performance decay or deactivation by irreversible oxidation reaction during catalytic process (Guo et al., 2017). In our design of multi-shelled hollow microsphere spinel catalysts in cubic phase, the high-energy-density structures were created by combining the active Co^{3+} and the precipitated intermediate Mn_7O_{13}. The strong interactions between binary metal oxides facilitate the generation of highly coordinated Mn-O-Co bonds and form high-oxidation-state manganese oxide. Meanwhile, the architecture of multi-shelled hollow microsphere offers attractive stability to resist high temperature, and large surface area to promote gas-solid interactions enhancing catalytic activity.

As the reaction time usually plays an important role in producing mesoporous microspheres and influences the final yield of the products, the morphological evolution as a function of the reaction time was evaluated with TEM analysis (Figure S5). By applying Co_2MnO-C as an example, it was observed that Co_2MnO-C microsphere without visible pores was formed at the initial stage. After the reaction time was elevated to 3 h, a yolk-shell structure that combined a porous shell and retained the dense core of glycerate-CoMn was observed. When the reaction time was further increased to 7 h, the solid sphere in the interior slowly shrank into a small microsphere with mesoporous structure in the same way. Thus, a unique multi-shelled Co_2MnO-C microsphere was finally obtained. In general, $Co_xMn_yO_4$ spinel nanoparticles possess low surface areas (no more than 80 m^2/g). Through a facile and rapid synthetic method, Chen and co-workers developed a series of granular $Co_xMn_yO_4$ with very high surface areas (122 m^2/g) (Chen et al., 2011). Comparatively, our multi-shelled Co_2MnO-C sample synthesized by the template-free method possessed the highest surface area of 203.5 m^2/g known up to now (Table S1 and Figures 3A and 3B), which was approximately twice those of $Co_xMn_yO_4$ spinel nanoparticles in previous literatures (Chen et al., 2011; Li et al., 2015a). Moreover, the surface areas of reported single-component Fe_2O_3, MoS_2, and V_2O_5 hollow microspheres constituted by 2D nanosheets were only 88.6, 31.5, and 60 m^2/g (Ma et al., 2015; Wang et al., 2016; Pan et al., 2013), which were several times lower than those of our prepared Co_2MnO-C sample. The results reveal that complex hollow microspheres formed by multi-component nanosheets can greatly enhance the surface area, which may be beneficial to CO oxidation. Unlike reported template approaches, here cobalt manganese spinel multi-shelled hollow microspheres were produced by a facile and template-free manner with no need for additional templates, extra multi-steps, and prolonged time. Comparatively, although Ostwald ripening procedure is considered as a useful template-free method and employed frequently to synthesize inorganic hollow spheres, it only focuses on certain special materials. Because of the anisotropy in different nanomaterials, it is very hard to assemble multi-component metal oxides into hierarchical hollow microspheres by simultaneously incorporating different components during synthesis process (Yu et al., 2017). Therefore, the strategy described here can be an effective and universal way for the controlled fabrication of various bimetallic spinel hollow microspheres.

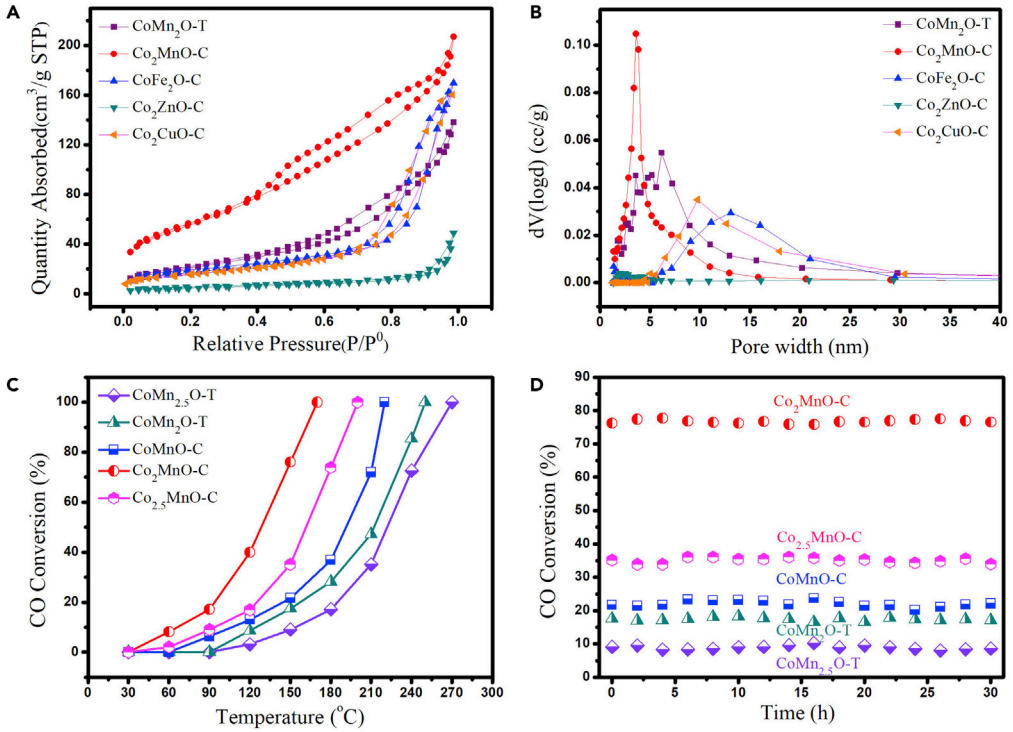

Figure 3. Specific Surface Area of Different Multi-shell Hollow Microspheres and CO Oxidation Catalysis under Moisture-Rich Conditions

(A and B) Adsorption/desorption isotherms (A) and Barrett-Joyner-Halenda (BJH) pore size distribution (B) for different kinds of spinel hollow microspheres. See also Table S1 and Figure S5.

(C) The catalytic activities of different $Co_xMn_yO_4$ samples for CO oxidation under moisture-rich conditions (~2% H_2O). See also Figure S8.

(D) Long-term durability test of as-prepared $Co_xMn_yO_4$ spinel catalysts under moisture-rich conditions (~2% H_2O). See also Figures S11 and S12.

On the basis of our synthetic route, other cobalt-based spinel multi-shelled hollow microspheres with high surface areas and mesoporous structure, such as $Co_xFe_yO_4$, $Co_xZn_yO_4$, and $Co_xCu_yO_4$, were also successfully synthesized (Figure S6). Moreover, 2D nanoflakes as secondary units were directly assembled into hierarchical bimetallic hollow structures, which greatly enhanced their surface areas and numbers of active sites and prevented self-aggregation behavior of low-dimensional subunits. In general, higher surface area can contribute to higher catalytic activity due to more exposed active sites and weakened metal-oxygen bond strength (Yan et al., 2013). For this reason, a catalytic experiment toward CO oxidation was carried out to clarify the relationship between the performance and structure. As expected, the catalytic activity in carbon monoxide oxidation followed the same tendency as the surface area (Figure S7). The amount of active sites can be enhanced with the increase of generated small pores, therefore the formed mesoporous structure greatly improved the mass transfer and led to the much better catalytic performance.

CO Oxidation Catalysis

The catalytic activity tests of all prepared spinel microspheres were carried out for CO catalytic oxidation. As depicted in the Figure S8, hierarchical Co_2MnO-C microsphere exhibits the highest activity among all samples in the temperature range of 30°C–90°C and the lowest apparent activation energy (30.1 kJ/mol) toward CO oxidation, which is fixed by the corresponding Arrhenius plots. Co_2MnO-C sample also gives specific rates of 54.95% conversion at 90°C, which is 15 times higher than that of $CoMn_2O$-T and at least two orders of magnitude more active than that of $CoMn_{2.5}O$-T catalyst. The Co_2MnO-C multi-shelled hollow microsphere possesses a high value of turnover frequencies (TOFs) (9.52×10^{-4} s^{-1}), which is 10 times more active than Co_3O_4 hollow microsphere (Figure S9), indicating the synergistic effect in $Co_xMn_yO_4$ spinel catalysts. The high activity at low temperature is consistent with the US Department of Energy

road map, which gives the aim for light off below 150°C (USDRIVE, 2013). The incorporation of Mn enhances the catalytic activity, which reaches the highest point at Co/Mn = 2:1, creating bimetallic spinel oxide catalyst with largely improved surface atom fractions, which consequently leads to high catalytic activity. Moreover, the performance of other bimetallic spinel nanostructures, in which Fe, Zn, and Cu were incorporated as major constituents, was also evaluated in the experiment. The results showed that these spinel catalysts were at least four times less active than Co_2MnO-C sample (Figure S10). The durability tests were used to explore the stability of the high-efficiency state of synthesized spinel catalysts; the as-prepared Co_2MnO-C samples can sustain the total conversion at 120°C for a long period of 71 h with similar morphology to that of the pristine samples under dry feed gas condition (Figures S11 and S12), showing superior stability compared with synthesized Co_2MnO-C solid microspheres, which failed in keeping the conversion after 19 h (Figure S13). Furthermore, although the prepared catalysts were deactivated after operation owing to the formation of formate or carbonate-like species (Figure S14) (Li et al., 2015b; Poyraz et al., 2013), the high activity with 100% CO conversion can be easily renewed and kept for at least up to five cycles by subsequent regenerations after oxidation treatment (Figure S15).

Metal oxides with complex structures or rich morphologies have recently been explored for catalytic oxidation applications. Examples include Co_3O_4 nanorods, Co_3O_4/graphene nanocomposites, integrated spinel nanoarrays, interfacial Pt-NiO_{1-x} nanostructures, Pt@$mSiO_2$ core-shell nanospheres, and nickel-iron foams (Xie et al., 2009; Lu and Zhao, 2015; Ren et al., 2014; Liang et al., 2011; Joo et al., 2009; Kim et al., 2018; Wang et al., 2012). Our present design of bimetallic spinel oxide multi-shelled hollow microspheres with wide tailorability and functionality enables the reactive molecules to directly enter their interior space by offering more open channels and less diffusion obstruction so as to take full advantage of highly exposed active sites and enhanced synergetic effect of components in such mixed metal oxides. In addition, the blockage of active sites and the conversion of surface lattice oxygen to hydroxy groups caused by the adsorption of water molecules are cut down to a large extent in the presence of Mn (Tao et al., 2019). The interactions between adsorbed CO and hydroxyl group on the surface were greatly weakened, which prevented the usually inevitable deactivation in CO oxidation reaction by trace concentrations of moisture, exhibiting great potential for practical use in oxidation reactions.

Water-Resisting Property of Cobalt Manganese Spinel Hollow Nanostructured Catalysts

In practice, metal oxide-based exhaust treatment catalysts are normally not water tolerant. Water-induced deactivation of the oxide catalysts still remains a big problem, especially for cobalt-based nanocatalysts. H_2O dissociative adsorption occurred in the oxygen vacancies and Co^{3+}, resulting in the formation of carbonates (Xie et al., 2009; Song et al., 2014). To evaluate water-resisting property of the prepared spinel nanocatalysts, the deactivation behavior was investigated in the presence of water conditions (~2% water vapor) (Figure 3C). Even though the existence of H_2O in feed gas lowered the conversion of CO, Co_2MnO-C multi-shelled hollow microsphere catalysts can still reach a total conversion at 170°C in moisture-rich conditions. By enhancing the content of Mn, the adsorbed H_2O decreases, which is evidenced by Fourier transform infrared spectroscopy (FTIR) analysis and water adsorption experiments (Figures S16 and S17). Therefore, we suppose that the behaviors of H_2O direct dissociation and adsorption on the oxygen vacancies and metal cations (Co or Mn) can be reduced, thus ensuring the availability of active sites for the adsorption of CO; this phenomenon is similar to the reported literature (Tao et al., 2019). As mentioned above, Co_2MnO-C multi-shelled hollow microsphere catalysts reached a total conversion at 120°C in normal conditions, therefore the difference between reaction temperature of complete oxidation in normal and moisture environment (ΔT) was as small as 50°C. After the incorporation of Mn in the formation of multi-shelled hollow microspheres, more active sites and surface defects were generated, thus increasing the reactivity of surface-adsorbed oxygen species and promoting their catalytic activity even under moisture-rich conditions. Compared with literature findings, Xie and co-workers synthesized very-high-activity Co_3O_4 nanorods with predominantly exposed {110} planes; however, the ΔT of Co_3O_4 nanorods catalysts was as large as 277°C (Xie et al., 2009). Meanwhile, the ΔT of most reported spinel nanoparticles was also very high and in the range of 100°C–178°C (Table S2) (Song et al., 2014; Kuo et al., 2014; Shen et al., 2017; Wang et al., 2014; Yu et al., 2009; Biemelt et al., 2016). Comparatively, the ΔT values of our $Co_xMn_yO_4$ sample can reach as low as 20°C, exhibiting the excellent water-resistent ability of $Co_xMn_yO_4$ multi-shelled hollow microsphere catalysts. Apart from these, despite the fact that the conversion of CO was reduced in the presence of water conditions, the prepared Co_2MnO-C multi-shelled hollow microsphere catalysts can still keep very high activity (TOF = $1.75\times10^{-4}\ s^{-1}$) among reported metal oxide and noble metal catalysts under moisture-rich conditions. Moreover, the as-prepared $Co_xMn_yO_4$ spinel catalysts showed long-term stability

in the presence of steam and maintained the activity with little fluctuation for as long as 30 h (Figure 3D). Compared with the performance of reported spinel-type catalysts, which often decayed in the first 10 h (Shen et al., 2017; Wang et al., 2014), the results demonstrated that as-prepared cobalt manganese spinel multi-shelled hollow microsphere catalysts were much more stable and very promising for practical application. The robust shield of bistratal shells can effectively retard the water poisoning, thus preserving high catalytic efficiency during CO oxidation, even under moisture-rich conditions.

The excellent catalytic performance of cubic $Co_xMn_yO_4$ spinel microsphere catalysts is considered to originate from their unique structural features and the preferred growth of $Co_xMn_yO_4$ spinel crystals, which gives the orientation to study the catalytic activity toward CO oxidation with different exposed planes. As trivalent cobalt ions play an important role in the catalytic activity for CO oxidation (Xie et al., 2009; Song et al., 2014), the big difference in performance between tetragonal and cubic $Co_xMn_yO_4$ spinel hollow microspheres can be explained by the amount of Co^{3+} that is easily oxidized. The preferential orientation of cubic Co_2MnO-C sample is $[\bar{1}10]$ or $[1\bar{1}0]$ direction; the {110} facet in one cubic spinel unit contains 8 Co atoms and 4 Mn atoms in theoretical models. The content of cobalt is higher than that of exposed tetragonal {010}, {112}, and cubic {112} planes in cobalt manganese spinels, which contain 2, 2, and 4 cobalt atoms, respectively. The results demonstrated that the cubic Co_2MnO-C exposed {110} facet possessed richer Co sites, which were highly effective sites for CO oxidation as confirmed both theoretically and experimentally. The chemical state of coordinated metal species in prepared mesoporous $Co_xMn_yO_4$ spinel multi-shelled hollow microspheres was evaluated by XPS analysis (Figures S18 and S19). Taking two representative spinel microspheres ($CoMn_2O$-T and Co_2MnO-C) as an example, two peaks of Co 2p3/2 and Co 2p1/2 are located around 781.4 and 796.6 eV, respectively, indicating the co-existence of two types of cobalt ions in tetragonal and cubic phase. The spectra of Co 2p (Figures S19A and S19B) reveal higher Co^{3+} concentration in Co_2MnO-C microspheres. In general, for cobalt-based catalysts, a high amount of trivalent cobalt ions often contributes to better catalytic performance due to more exposed active sites. However, it was found that, although $Co_{2.5}MnO$-C spinel multi-shelled hollow microspheres possessed the highest packs of Co^{3+}, it was not the most active catalyst. Therefore the catalytic activity was determined not only by the number of Co^{3+} but also by the point defect concentration.

An important feature of physicochemical properties underlying structure formation is reflected by the variation of the defects in crystal lattice (Huang, 2016; Hu et al., 2016). To further understand the mechanisms, the oxygen vacancy concentration was further adjusted by controlling the crystal phase and plane lattice parameter of $Co_xMn_yO_4$ spinel microspheres. Based on the TEM analysis in Figure 2, physical models of four kinds of crystal facets, {010} and {112} in tetragonal phase and {110} and {112} in cubic phase, are depicted in Figure 4A. The defects of microsphere samples are evaluated by FTIR. The bands at 617 cm^{-1} can be assigned to vibration of atoms in tetrahedral oxygen environment related to the Mn-O in spinels, whereas the absorptions at about 515 cm^{-1} are attributable to the Co-O stretching vibrations in the octahedral oxygen environment (Figure 4G) (Tholkappiyan et al., 2015). The stretching bands of Mn-O and Co-O shift to 658 cm^{-1} and 570 cm^{-1} with the increase of Co/Mn molar ratio to 2. The result reflects the generation of Kirkendall voids on completion of the reaction, which is evidenced by the TEM images (Figures 4B–4F). It is worth to note that the Mn-O and Co-O vibration peaks shift to the right side after further enhancing the cobalt content in catalysts, illustrating the decrement of defect concentrations in $Co_{2.5}MnO$-C sample. As usual, oxygen vacancies are thought to be the best active sites for oxygen activation (Zhao et al., 2013), the fitted O 1s spectra displaying four major oxygen contributions with the corresponding peaks are depicted in Figures 4H and S20. The Co_2MnO-C sample exhibits the most abundant oxygen vacancies (14.72%) on the surface (Table S3) and the reactivity of surface-adsorbed oxygen species is greatly enhanced. As XPS analysis performed under vacuum can contribute to the formation of oxygen vacancies, we employed the ambient pressure X-ray photoelectron spectroscopy (APXPS) instrument to evaluate the actual content of oxygen vacancies. The results demonstrated that the content of oxygen vacancies under vacuum condition was only a little higher that of oxygen vacancies analyzed under ambient conditions (Tables S3 and S4). It is also observed that the concentration of oxygen vacancies for these facets follows the order: C-{110}>C-{112}>T-{010}>T-{112}. Because the planes of CoMnO-C and $Co_{2.5}MnO$-C are the same, the lattice oxygen mobility is lower than that of Co_2MnO-C catalyst, which is in agreement with FTIR analysis. Figure 4I illustrates the cobalt and manganese cations and oxygen vacancies at atom scale; the lattice oxygen migration can easily be promoted on the surface of {110} facet of cubic phase Co_2MnO-C due to the high oxygen vacancy formation energies.

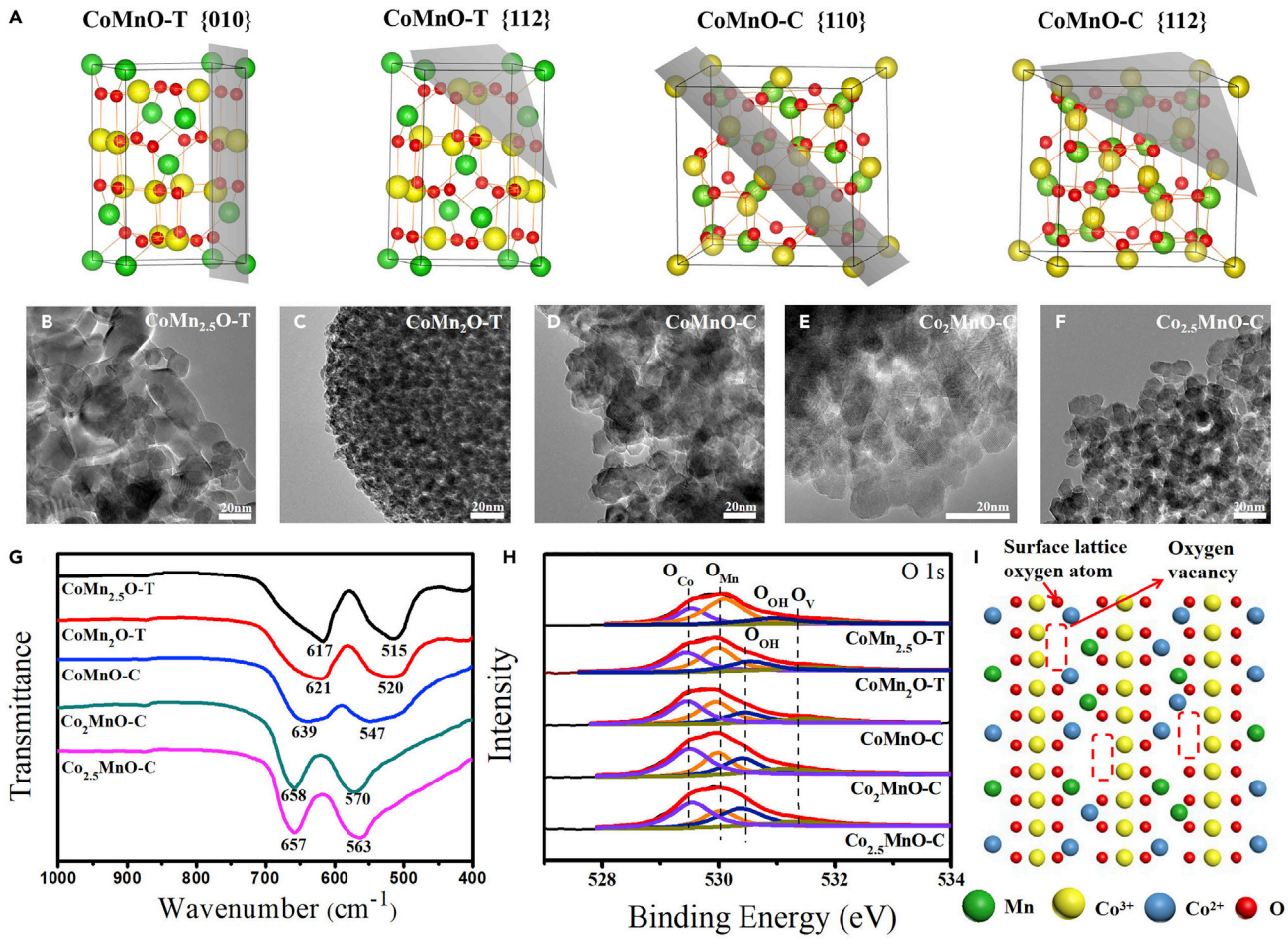

Figure 4. Structural Characterization of $Co_xMn_yO_4$ Spinel Hollow Microsphere Catalysts

(A) Theoretical models of the different planes of $Co_xMn_yO_4$ spinel hollow microspheres with tetragonal and cubic phases. See also Figures S21.

(B–F) TEM images of as-prepared $Co_xMn_yO_4$ spinel samples showing crystal surfaces and internal voids.

(G and H) FTIR spectra and APXPS spectra of O 1s peaks for as-prepared $Co_xMn_yO_4$ spinel catalysts. See also Table S4.

(I) Schematic showing the surface of Co_2MnO-C spinel catalyst.

The Mars-van Krevelen (MvK) mechanism has been widely used to describe the CO oxidation reaction (Widmann and Behm, 2014; Nyathi et al., 2019). CO oxidation on prepared cobalt manganese spinels also follows the MvK mechanism, the details of which are as follows. A CO molecule interacts with a lattice oxygen in $Co_xMn_yO_4$ to generate CO_2, instead of directly reacting with the gas-phase O_2, leaving an oxygen vacancy on the surface. Oxygen vacancies on catalyst surfaces may have a promotion effect on increasing catalytic activity. Because of the activation of the O_2 at lattice vacancies, the gas-phase O_2 participates in a reaction only after a rain check (Wu et al., 2014). Then the gas-phase O_2 molecules are adsorbed at the oxygen vacancy sites. Subsequently, another CO molecule interacts with the adsorbed O_2, generating CO_2 and regenerating the surface. For catalysts with high efficiency, the catalytic active site needs to adsorb the reactant fast and desorb the product fast too. Therefore, the interaction between gas molecules (CO or CO_2) and cobalt manganese spinels has great importance in determining the catalytic activity. We took molecular dynamics simulations by using the Materials Studio software package to calculate the interaction energies between gas molecules and cobalt manganese spinel exposed different facets. On account of XRD and HRTEM analysis, four kinds of models of tetragonal phase {010} and {112} surface and cubic phase {110} and {112} surface are constructed with optimized structural properties. The results demonstrated that the interaction energy (−4.66 kcal/mol) between polar CO molecules and Co_2MnO-C exposed {110} plane was the strongest among established models (Table S5), revealing the strong electrostatic interaction and that the CO molecules were more easily captured on the {110} plane in the Co_2MnO-C sample. We also simulated the adsorption of CO molecules by putting

the models of cobalt manganese spinels into an atmosphere of gas molecules. As depicted in Figure S21, the cubic Co_2MnO_4 sample with exposed {110} plane exhibits faster capture of CO molecules than other samples, achieving almost complete adsorption in 5 ns. On the other hand, the rate of desorption is also very important in enhancing catalytic performance. The calculated interaction energy (−0.31 kcal/mol) between nonpolar CO_2 molecules and Co_2MnO-C exposed {110} was the weakest, illustrating that CO_2 molecules could easily overcome the barriers to desorb on {110} plane. Moreover, Co_2MnO-C sample exhibited the most abundant oxygen vacancies (14.35%) on the surface evidenced by APXPS analysis; the lattice oxygen mobility was greatly enhanced. From the above, the high adsorption of CO and fast desorption rate for CO_2, as well as abundant oxygen vacancies, endowed the Co_2MnO-C sample with high catalytic activity toward CO oxidation.

Conclusion

We have developed a simple and efficient methodology for the template-free production of hierarchical multi-shelled hollow nanostructured catalysts from cobalt-based bimetallic spinels. Through precise control of architecture and composition, the self-assembled robust microspheres configured by 16-nm $Co_xMn_yO_4$ nanosheets demonstrated large surface area, favorable surface chemistry, and abundant oxygen vacancies (14.35%), which led to excellent catalytic performance in catalytic oxidation reactions at low temperature. In the meantime, as-prepared non-precious $Co_xMn_yO_4$ spinel catalysts exhibited most attractive water-resisting property for low-temperature CO oxidation and can keep very high activity (TOF = 1.75×10^{-4} (s^{-1})) for as long as 30 h in the presence of steam, surpassing by far the best performance of all spinel nanoparticle catalysts reported in the literature. As well as being interesting in itself and cost efficient in practical application, the methodology can also be extended to design other stable mixed transition metal oxide systems with various configurations and compositions.

Limitations of the Study

So far, it has been very difficult to quantitatively analyze the specific reaction process of catalytic reaction on molecular scale by characterizations. Therefore, theoretical calculation was carried out by establishing models to further describe the reaction mechanism. Although the atomic-level models were established to make a qualitative description about the interactions between gas molecules and cobalt manganese spinel exposed different facets, more desirable theoretical models are needed for quantitatively illustrating the reaction mechanism.

METHODS

All methods can be found in the accompanying Transparent Methods supplemental file.

SUPPLEMENTAL INFORMATION

Supplemental Information can be found online at https://doi.org/10.1016/j.isci.2019.10.013.

ACKNOWLEDGMENTS

This work was supported by the National Natural Science Foundation of China (No. 21236008, 21736009 and 21808202), the Zhejiang Provincial Natural Science Foundation of China (Grant No. LY18B060010), Minjiang Scholarship from Fujian Provincial Government, and Postdoctoral Science Foundation of China (2018M642480). We thank J.Z. He for useful discussion and the independent measurement of spinel composition and structure.

AUTHOR CONTRIBUTIONS

G.Z. and Z. Xu conceived the research idea. Z. Xu, Y.Z., X.L., L.Q., Z.F., and Z. Xue synthesized the cobalt manganese spinel materials and related multi-shelled hollow nanostructured catalysts. Z. Xu, Y.Z., Q.M., C.S., Q. Liu, X.G., B.M., and Z.L. carried out related characterizations, measurements, and calculations. G.Z. and Q. Li contributed to the general methodology. Y.Z. and Q.M. reviewed the manuscript. G.Z. supervised the project, helped design the experiments, and co-drafted the manuscript. All authors contributed to the analysis of the manuscript.

DECLARATION OF INTERESTS

The authors declare no competing interests. A patent application related to this work has been filed.

Received: June 23, 2019
Revised: September 16, 2019
Accepted: October 2, 2019
Published: November 22, 2019

REFERENCES

Biemelt, T., Wegner, K., Teichert, J., Lohe, M.R., Martin, J., Grothe, J., and Kaskel, S. (2016). Hopcalite nanoparticle catalysts with high water vapour stability for catalytic oxidation of carbon monoxide. Appl. Catal. B *184*, 208–215.

Bragg, W.H. (1915). The structure of magnetite and spinels. Nature *95*, 561.

Cargnello, M., Doan-Nguyen, V.V.T., Gordon, T.R., Diaz, R.E., Stach, E.A., Gorte, R.J., Fornasiero, P., and Murray, C.B. (2013). Control of metal nanocrystal size reveals metal-support interface role for ceria catalysts. Science *341*, 771–773.

Cargnello, M., Jaen, J.J.D., Garrido, J.C.H., Bakhmutsky, K., Montini, T., Gamez, J.J.C., Gorte, R.J., and Fornasiero, P. (2012). Exceptional activity for methane combustion over modular Pd@CeO2 subunits on functionalized Al2O3. Science *337*, 713–717.

Chen, C.H., Njagi, E.C., Sun, S.P., Genuino, H., Hu, B., and Suib, S.L. (2010). Hydrophobic polymer-coated metal oxide catalysts for effective low-temperature oxidation of CO under moisture-rich conditions. Chem. Mater. *22*, 3313–3315.

Chen, F., Shen, J., Peng, B., Pan, Y., Tao, Z., and Chen, J. (2011). Rapid room-temperature synthesis of nanocrystalline spinels as oxygen reduction and evolution electrocatalysts. Nat. Chem. *3*, 79–84.

Christopher, P., Xin, H., and Linic, S. (2011). Visible-light-enhanced catalytic oxidation reactions on plasmonic silver nanostructures. Nat. Chem. *3*, 467–472.

Dai, C., Zhang, A., Liu, M., Guo, X., and Song, C. (2015). Hollow ZSM-5 with silicon-rich surface, double shells, and functionalized interior with metallic nanoparticles and carbon nanotubes. Adv. Funct. Mater. *25*, 7479–7487.

de la Cruz, C., Huang, Q., Lynn, J.W., Li, J.Y., Ratcliff, W., Zarestky, J.L., Mook, H.A., Chen, G.F., Luo, J.L., Wang, N.L., and Dai, P.C. (2008). Magnetic order close to superconductivity in the iron-based layered $LaO_{1-x}F_xFeAs$ systems. Nature *453*, 899–902.

Goodman, E.D., Dai, S., Yang, A., Wrasman, C.J., Gallo, A., Bare, S.R., Hoffman, A.S., Jaramillo, T.F., Graham, G.W., Pan, X., and Cargnello, M. (2017). Uniform Pt/Pd bimetallic nanocrystals demonstrate platinum effect on palladium methane combustion activity and stability. ACS Catal. *7*, 4372–4380.

Guo, C., Zheng, Y., Ran, J., Xie, F., Jaroniec, M., and Qiao, S. (2017). Engineering high-energy interfacial structures for high-performance oxygen-involving electrocatalysis. Angew. Chem. Int. Ed. *129*, 1–6.

Gu, D., Jia, C., Weidenthaler, C., Bongard, H., Spliethoff, B., Schmidt, W., and Schüth, F. (2015). Highly ordered mesoporous cobalt-containing oxides: structure, catalytic properties, and active sites in oxidation of carbon monoxide. J. Am. Chem. Soc. *137*, 11407–11418.

Hu, J., Chen, M., Fang, X., and Wu, L. (2011). Fabrication and application of inorganic hollow spheres. Chem. Soc. Rev. *40*, 5472–5491.

Hu, L., Peng, Q., and Li, Y. (2008). Selective synthesis of Co_3O_4 nanocrystal with different shape and crystal plane effect on catalytic property for methane combustion. J. Am. Chem. Soc. *130*, 16136–16137.

Hu, Z., Liu, X., Meng, D., Guo, Y., Guo, Y.L., and Lu, G. (2016). Effect of ceria crystal plane on the physicochemical and catalytic properties of Pd/ceria for CO and propane oxidation. ACS Catal. *6*, 2265–2279.

Huang, W. (2016). Oxide nanocrystal model catalysts. Acc. Chem. Res. *49*, 520–527.

Indra, A., Menezes, P.W., Sahraie, N.R., Bergmann, A., Das, C., Tallarida, M., Schmeisser, D., Strasser, P., and Driess, M. (2014). Driess, Unification of catalytic water oxidation and oxygen reduction reactions: amorphous beat crystalline cobalt iron oxides. J. Am. Chem. Soc. *136*, 17530–17536.

Joo, S.H., Park, J.Y., Tsung, C., Yamada, Y., Yang, P., and Somorjai, G.A. (2009). Thermally stable Pt/mesoporous silica core-shell nanocatalysts for high-temperature reactions. Nat. Mater. *8*, 126–131.

Kim, J., Park, W.H., Doh, W.H., Lee, S.W., Noh, M.C., Gallet, J., Bournel, F., Kondoh, H., Mase, K., Jung, Y., et al. (2018). Adsorbate-driven reactive interfacial Pt-NiO_{1-x} nanostructure formation on the $Pt_3Ni(111)$ alloy surface. Sci. Adv. *4*, eaat3151.

Kuo, C.H., Li, W., Song, W., Luo, Z., Poyraz, A.S., Guo, Y., Ma, A.W.K., Suib, S.L., and He, J. (2014). Facile synthesis of Co_3O_4@CNT with high catalytic activity for CO oxidation under moisture-rich conditions. ACS Appl. Mater. Interfaces *6*, 11311–11317.

Lavela, P., Tirado, J.L., and Vidal-Abarca, C. (2007). Vidal-Abarca, Sol-gel preparation of cobalt manganese mixed oxides for their use as electrode materials in lithium cells. Electrochim. Acta *52*, 7986–7995.

Li, J., Liang, X., Xu, S., and Hao, J. (2009). Catalytic performance of manganese cobalt oxides on methane combustion at low temperature. Appl. Catal. B *90*, 307–312.

Li, Y., and Shi, J. (2014). Hollow-structured mesoporous materials: chemical synthesis, functionalization and applications. Adv. Mater. *26*, 3176–3205.

Li, C., Han, X., Cheng, F., Hu, Y., Chen, C., and Chen, J. (2015a). Phase and composition controllable synthesis of cobalt manganese spinel nanoparticles towards efficient oxygen electrocatalysis. Nat. Commun. *6*, 7345.

Li, Q., Xie, W., Chen, G., Li, Y., Huang, Y., and Chen, X. (2015b). The behaviors of ultra-low-gold-loaded catalysts (Au/CeO_2) for CO oxidation in the presence of water on the catalysts. Nano Res. *8*, 3075–3084.

Li, G., Wang, X., Fu, J., Li, J., Park, M., Zhang, Y., Lui, G., and Chen, Z. (2016a). Pomegranate-inspired design of highly active and durable bifunctional electrocatalysts for rechargeable metal-air batteries. Angew. Chem. Int. Ed. *55*, 4977–4982.

Li, W., Zhang, Y., Xu, Z., Meng, Q., Fan, Z., Ye, S., and Zhang, G. (2016b). Assembly of MOF microcapsules with size-selective permeability on cell walls. Angew. Chem. Int. Ed. *55*, 955–959.

Li, W., Zhang, Y., Zhang, C., Meng, Q., Xu, Z., Su, P., Li, Q., Shen, C., Fan, Z., Qin, L., and Zhang, G. (2016c). Transformation of metal-organic frameworks for molecular sieving membranes. Nat. Commun. *7*, 11315.

Liang, Y., Li, Y., Wang, H., Zhou, J., Wang, J., Regier, T., and Dai, H. (2011). Co_3O_4 nanocrystals on graphene as a synergistic catalyst for oxygen reduction reaction. Nat. Mater. *10*, 780–786.

Lu, J., Zhan, C., Wu, T., Wen, J., Lei, Y., Kropf, A., Wu, H., Miller, D., Elam, J., Sun, Y., et al. (2014). Effectively suppressing dissolution of manganese from spinel lithium manganate via a nanoscale surface-doping approach. Nat. Commun. *5*, 5693.

Lu, X., and Zhao, C. (2015). Electrodeposition of hierarchically structured three-dimensional nickel-iron electrodes for efficient oxygen evolution at high current densities. Nat. Commun. *6*, 7616.

Ma, F., Hu, H., Wu, H.B., Xu, C.Y., Xu, Z., Zhen, L., and Lou, X.W. (2015). Formation of uniform Fe_3O_4 hollow spheres organized by ultrathin nanosheets and their excellent lithium storage properties. Adv. Mater. *27*, 4097–4101.

Menezes, P.W., Indra, A., Sahraie, N.R., Bergmann, A., Strasser, P., and Driess, M. (2015). Cobalt-manganese-based spinels as multifunctional materials that unify catalytic water oxidation and oxygen reduction reactions. Chemsuschem *8*, 164–171.

Nie, L., Mei, D., Xiong, H., Peng, B., Ren, Z., Hernandez, X.I.P., DeLariva, A., Wang, M., Engelhard, M.H., Kovarik, L., et al. (2017). Activation of surface lattice oxygen in single-atom Pt/CeO_2 for low-temperature CO oxidation. Science *358*, 1419–1423.

Nyathi, T.M., Fischer, N., York, A.P.E., Morgan, D.J., Hutchings, G.J., Gibson, E.K., Wells, P.P.,

Catlow, C.R.A., and Claeys, M. (2019). Impact of nanoparticle-support interactions in Co_3O_4/Al_2O_3 catalysts for the preferential oxidation of carbon monoxide. ACS Catal. *9*, 7166–7178.

Pan, A.Q., Wu, H.B., Zhang, L., and Lou, X.W. (2013). Uniform V_2O_5 nanosheet-assembled hollow microflowers with excellent lithium storage properties. Energy Environ. Sci. *6*, 1476–1479.

Poizot, P., Laruelle, S., Grugeon, S., Dupont, L., and Tarascon, J.M. (2000). Tarascon Nano-sized transition-metal oxides as negative-electrode materials for lithium-ion batteries. Nature *407*, 496–499.

Poyraz, A.S., Kuo, C.-H., Biswas, S., King'ondu, C.K., and Suib, S.L. (2013). A general approach to crystalline and monomodal pore size mesoporous materials. Nat. Commun. *4*, 2952.

Ren, Z., Botu, V., Wang, S.B., Meng, Y.T., Song, W.Q., Guo, Y.B., Ramprasad, R., Suib, S.L., and Gao, P.X. (2014). Monolithically integrated spinel $M_xCo_{3-x}O_4$ (M=Co, Ni, Zn) nanoarray catalysts: scalable synthesis and cation manipulation for tunable low-temperature CH_4 and CO oxidation. Angew. Chem. Int. Ed. *53*, 7223–7227.

Saavedra, J., Pursell, C., and Chandler, B. (2018). CO oxidation kinetics over Au/TiO_2 and Au/Al_2O_3 catalysts: evidence for a common water-assisted mechanism. J. Am. Chem. Soc. *140*, 3712–3723.

Shen, Y., Yu, J., Xiao, X., Guo, X., Mao, D., Huang, H., and Lu, G. (2017). Polymer nanofilm-coated catalysis: an approach for enhancing water resistance of Co-Fe oxide nano-catalysts under moisture-rich condition. J. Catal. *352*, 466–479.

Song, W., Poyraz, A.S., Meng, Y., Ren, Z., Chen, S.Y., and Suib, S.L. (2014). Mesoporous Co_3O_4 with controlled porosity: inverse micelle synthesis and high-performance catalytic CO oxidation at -60 °C. Chem. Mater. *26*, 4629–4639.

Tao, L., Zhang, Z., Chen, P., Zhao, G., Liu, Y., and Lu, Y. (2019). Thin-felt Al-fiber-structured Pd-Co-MnO_x/Al_2O_3 catalyst with high moisture resistance for high-throughput O_3 decomposition. Appl. Surf. Sci. *481*, 802–810.

Tholkappiyan, R., Naveen, A.N., Sumithra, S., and Vishista, K. (2015). Investigation on spinel $MnCo_2O_4$ electrode material prepared via controlled and uncontrolled synthesis route for supercapacitor application. J. Mater. Sci. *50*, 5833–5843.

USDRIVE. (2013). Advanced combustion and emission control roadmap. http://www1.eere.energy.gov/vehiclesandfuels/pdfs/program/acec_roadmap_ june2013. pdf.

Vila, E., Rojas, R.M., Martín de Vidales, J.L., and García-Martínez, O. (1996). Structural and thermal properties of the tetragonal cobalt manganese spinels $Mn_xCo_{3-x}O4$ (1.4<x<2.0). Chem. Mater. *8*, 1078–1083.

Wang, H., Kavanagh, R., Guo, Y.L., Guo, Y., Luo, G.Z., and Hu, P. (2012). Structural origin: water deactivates metal oxides to CO oxidation and promotes low-temperature CO oxidation with metals. Angew. Chem. Int. Ed. *51*, 6657–6661.

Wang, Y., Yu, L., and Lou, X.W. (2016). Synthesis of highly uniform molybdenum-glycerate spheres and their conversion into hierarchical MoS_2 hollow nanospheres for lithium-ion batteries. Angew. Chem. Int. Ed. *55*, 7423–7426.

Wang, Y., Zhu, X., Crocker, M., Chen, B., and Shi, C. (2014). A comparative study of the catalytic oxidation of HCHO and CO over $Mn_{0.75}Co_{2.25}O_4$ catalyst: the effect of moisture. Appl. Catal. B *160-161*, 542–551.

Widmann, D., and Behm, R.J. (2014). Activation of molecular oxygen and the nature of the active oxygen species for co oxidation on oxide supported au catalysts. Acc. Chem. Res. *47*, 740–749.

Wiley, J.B., and Kaner, R.B. (1992). Rapid solid-state precursor synthesis of materials. Science *255*, 1093–1097.

Wu, Z., Jiang, D., Mann, A.K.P., Mullins, D.R., Qiao, Z., Allard, L.F., Zeng, C., Jin, R., and Overbury, S.H. (2014). Thiolate ligands as a double-edged sword for CO oxidation on CeO_2 Supported $Au_{25}(SCH_2CH_2Ph)_{18}$ Nanoclusters. J. Am. Chem. Soc. *136*, 6111–6122.

Wu, Z., Xu, S., Yan, Q., Chen, Z., Ding, Y., Li, C., Liang, H., and Yu, S.H. (2018). Transition metal-assisted carbonization of small organic molecules toward functional carbon materials. Sci. Adv. *4*, eaat0788.

Xie, X.W., Li, Y., Liu, Z.Q., Haruta, M., and Shen, W.J. (2009). Low-temperature oxidation of CO catalysed by Co_3O_4 nanorods. Nature *458*, 746–749.

Yan, N., Chen, Q., Wang, F., Wang, Y., Zhong, H., and Hu, L. (2013). High catalytic activity for CO oxidation of Co_3O_4 nanoparticles in SiO_2 nanocapsules. J. Mater. Chem. A *1*, 637–643.

You, B., Jiang, N., Sheng, M., Bhushan, M.W., and Sun, Y. (2016). Hierarchically porous urchin-like Ni_2P superstructures supported on nickel foam as efficient bifunctional electrocatalysts for overall water splitting. ACS Catal. *6*, 714–721.

Yu, L., Hu, H., Wu, H., and Lou, X. (2017). Complex hollow nanostructures: synthesis and energy-related applications. Adv. Mater. *29*, 1604563.

Yu, Y., Takei, T., Ohashi, H., He, H., Zhang, X., and Haruta, M. (2009). Pretreatments of Co_3O_4 at moderate temperature for CO oxidation at 80 °C. J. Catal. *267*, 121–128.

Zhang, G., and Lou, X.W. (2014). General synthesis of multi-shelled mixed metal oxide hollow spheres with superior lithium storage properties. Angew. Chem. Int. Ed. *126*, 9187–9190.

Zhang, K., Li, L., Shaikhutdinov, S., and Freund, H. (2018). Carbon monoxide oxidation on metal-supported monolayer oxide films: establishing which interface is active. Angew. Chem. Int. Ed. *57*, 1261–1265.

Zhao, K., Zhang, L., Wang, J., Li, Q., He, W., and Yin, J.J. (2013). Surface structure-dependent molecular oxygen activation of BiOCl single-crystalline nanosheets. J. Am. Chem. Soc. *135*, 15750–15753.

Zhao, Q., Yan, Z., Chen, C., and Chen, J. (2017). Spinels: controlled preparation, oxygen reduction/evolution reaction application, and beyond. Chem. Rev. *117*, 10121–10211.

ISCI, Volume *21*

Supplemental Information

Template-free Synthesis of Stable Cobalt Manganese Spinel Hollow Nanostructured Catalysts for Highly Water-Resistant CO Oxidation

Zehai Xu, Yufan Zhang, Xiong Li, Lei Qin, Qin Meng, Guoliang Zhang, Zheng Fan, Zhen Xue, Xinwen Guo, Qinglin Liu, Qingbiao Li, Baohua Mao, and Zhi Liu

Supplementary Information

Template-free synthesis of stable cobalt manganese spinel hollow nanostructured catalysts for highly water-resistant CO oxidation

Zehai Xu[1,8], Yufan Zhang [2,8], Xiong Li [1], Lei Qin[1], Qin Meng [3], Guoliang Zhang[1,5,9,*], Zheng Fan[1], Zhen Xue[1], Xinwen Guo[4], Qinglin Liu[5], Qingbiao Li [5,6,*], Baohua Mao[7], Zhi Liu[7]

[1] Institute of Oceanic and Environmental Chemical Engineering, State Key Lab Breeding Base of Green Chemical Synthesis Technology, Zhejiang University of Technology, Hangzhou 310014, P. R. China.

[2] Department of Mechanical Engineering, College of Engineering, Carnegie Mellon University, Pittsburgh, PA 15213, USA.

[3] College of Chemical and Biological Engineering, State Key Laboratory of Chemical Engineering, Zhejiang University, Hangzhou 310027, P. R. China.

[4] State Key Laboratory of Fine Chemicals, Department of Catalysis Chemistry and Engineering, Dalian University of Technology, Dalian 116012, P. R. China.

[5] College of Chemistry and Chemical Engineering, National Laboratory for Green Chemical Productions of Alcohols, Ethers and Esters, Xiamen University, Xiamen, 361005, P. R. China.

[6] Fujian Province Key Laboratory of Energy Cleaning Utilization and Development, Jimei University, Xiamen 361021, P. R. China.

[7] Shanghai Institute of Microsystem and Information Technology, Chinese Academy of Sciences, Shanghai 200050, China

[8] These authors contributed equally.

[9] Lead Contact.

*Correspondence: guoliangz@zjut.edu.cn; kelqb@xmu.edu.cn

Experimental details

Transparent Methods

Materials

Cobalt nitrate, manganous nitrate, zinc nitrate, ferric nitrate, cupric nitrate, glycerol and isopropanol were of analytical grade without further purification. All experiment solutions were prepared from deionized water manufactured by a self-made RO−EDI system, in which ion concentration was analyzed by IRIS Intrepid ICP and Metrohm 861Compact IC and controlled to meet $\sigma \leq 0.5$ μS cm^{-1}.

Preparation of $Co_xMn_yO_4$ spinel hollow microspheres.

All the chemicals were directly used after purchase without further purification. In a typical synthesis of cubic Co_2MnO-C sample, 0.0728g cobalt nitrate, 0.0314 g manganous nitrate and 8 ml of glycerol were added into 40 ml of isopropanol solution. The mixed solution was then transferred to a Teflon-lined stainless steel autoclave and kept at 180 ^oC. After cooling to room temperature naturally, the brown precipitate was separated by centrifugation, washed several times with ethanol and dried in an oven over night. The subsequent decomposition of glycerine-metal precursors was calcined in air at 500 ^oC with a ramp rate of 1 ^oC/min. Similarly, cubic CoMnO-C and $Co_{2.5}MnO$-C spinel hollow microspheres were obtained by adopting the corresponding stoichiometric amount of cobalt nitrate and manganous nitrate, respectively. Moreover, the tetragonal $CoMn_{2.5}O$-T and $CoMn_2O$-T samples were also prepared by tuning the molar ratio of Co:Mn.

Catalytic activity measurements.

The catalytic activities of different catalysts for CO oxidation were evaluated in a fixed bed quartz tubular reactor. Usually, most of nanocrystals need to be activated in oxidizing atmospheres at relatively high temperatures (>350 ^{o}C) prior to CO oxidation tests. Pretreatment in an oxidizing atmosphere has a chance of partially oxidizing the catalyst and the preadsorbed labile O_2 on the catalyst surface can enhance the oxidation of CO at low temperatures. Herein, we first took the pretreated catalysts under Ar flow so as to make the performance to be truly revealed in catalytic oxidation of CO. The powder samples were packed between quartz wool with a thermocouple placed touching the sample inside the reactor. Prior to the tests, the samples were pelletized and sieved to 40 and 60 mesh for use. The catalysts (100 mg) were pretreated under Ar flow at 200 ^{o}C for 2 h in advance. The reactant gases (1 vol.% CO, 1 vol.% O_2, balanced with nitrogen) went through the reactor at a rate of 60 mL min^{-1}, corresponding to a gas hourly space velocity (GHSV) of 36000 ml g^{-1} h^{-1}. The effluent gas compositions were analyzed on-line by a gas chromatograph (GC 1690) equipped with a thermal conductivity detector. Moisture rich condition (~2% water vapor) was acquired by passing the reactant gas through a water channel. The high temperature oxidation treatments of catalyst regeneration were set at 600 ^{o}C (1 vol.% O_2/Ar) for Co_2MnO-C samples, respectively.

Preparation of $Co_xFe_yO_4$, $Co_xZn_yO_4$ and $Co_xCu_yO_4$ spinel hollow microspheres. The processes were carried out in a similar way to the prepared other substituted cobalt-based spinels ($Co_xFe_yO_4$, $Co_xZn_yO_4$ and $Co_xCu_yO_4$) except that the molar ratio

and respective precursors. According to the compositions and XRD analysis of prepared microspheres, the bimetallic spinel samples were named as $CoFe_2O$-C, Co_2FeO-C, $CoZn_2O$-C, Co_2ZnO-C, $CoCu_2O$-C and Co_2CuO-C, respectively.

Field-emission scanning electron microscopy (FESEM)

A field-emission scanning electron microscope (FESEM) (S-4700, Hitachi, Japan) was used to observe the morphologies of the prepared catalysts. Accelerating voltage was 15 kV. All the prepared samples were coated with an ultrathin layer of platinum using an ion sputter coater to minimize charging effects.

Transmission electron microscopy (TEM)

Transmission electron microscopy (Hitachi, Japan) was performed at an accelerating voltage of 300 kV. The composition of the sample was determined by energy dispersive X-ray spectroscopy (EDX) experiments, which were carried out in the TEM. The prepared suspension was dropped on an ultrathin carbon films supported by copper net and dried overnight at atmosphere.

X-ray diffraction (XRD)

The crystalline structure of the as-synthesized materials was observed by X-ray diffraction (XRD). XRD patterns were recorded by a PNAlytical X' Pert PRO X-ray diffractometer with Cu K_α radiation (λ= 1.5418Å) at 40 kV and 40 mA. The samples were scanned using a step size of 0.02 º and a scan speed of 1 s per step in a continuous scanning mode. The data was collected for 2θ angles between 10 ° and 80 °.

X-ray photoelectron spectroscopy (XPS)

X-ray photoelectron spectroscopy (XPS) analysis were performed on a RBD upgraded PHI-5000C ESCA system (Perkin Elmer) with an incident radiation of monochromatic Mg Kα X-rays (hν=1253.6 eV) at 250 W. The high voltage was held at 14.0 kV. To ensure sufficient resolution and sensitivity, the pass energy was set as 46.95 eV. In analysis chamber, the pressure was put below 5×10^{-8} Pa. The spectra of all the elements were recorded by using RBD 147 interface (RBD Enterprises, USA). Moreover, in order to evaluate the content of oxygen vacancies, we employed a customized, lab-based ambient pressure X-ray photoelectron spectroscopy APXPS instrument (Specs Co.) to analyze the samples. The system was equipped with a monochromic aluminum K_α X-ray source and PHOIBOS 150 HV analyzer. XPS spectra of O 1s peaks were fitted into four major oxygen contributions, and the content of oxygen vacancies was calculated according to the ratio of peak areas.

N_2 adsorption characterization

N_2 adsorption-desorption isotherms were measured by a Micromeritics-Accelerated Surface Area and Porosimetry system (ASAP 2020M+C, Micromeritics Instrument Co., USA). Measurements were carried out at 77 K using a liquid nitrogen bath. The samples were degassed in vacuum at 150 ℃ for 12 h before analysis. Brunauer-Emmett-Teller method was used to calculate the specific surface areas in the P/P_0 range of 0.05-1.0. BJH method was used to obtain the pore-size distributions.

Fourier transform-infrared spectroscopy (FT-IR)

Fourier transform-infrared spectroscopy (FT-IR) spectra were carried out on a Nicolet 6700 spectrometer (Thermo Fisher Nicolet, USA) equipped with a TGS detector. 64 scans (8 cm^{-1} nominal resolution) were collected for one spectrum. Pellets were made by diluting samples with KBr.

Water adsorption experiments

Water adsorption experiments were carried out in a flow system with a rate of 60 mL min^{-1} for 3 h. The prepared catalysts (1 g) was put in a reactor tube at room temperature. The content of H_2O in reactor tube was controlled by passing the feed gas through a water channel. The amount of water uptake was calculated by weighing the catalysts before and after three water adsorption experiments.

Molecular dynamics simulations

The molecular dynamics simulations were carried out using the Materials Studio software package from Accelrys Incorporation (Wang et al. 2007). The model and force field of tetragonal and cubic cobalt manganese spinels were constructed with parameters derived from JCPDS 77-0471 and JCPDS 23-1237, respectively (Chen et al. 2011; Li et al. 2015a). For CO capture simulations, the calculations were carried out with CASTEP (Cambridge Sequential Total Energy Package) code. The generalized gradient approximation (GGA) was used in the scheme of PerdewBurke-Ernzerhof (PBE) to describe the exchange-correlation functional. Energy minimization method was applied to all systems and then a long 10 ns run was made with a NVT ensemble at 298 K. The used time step was 1 fs and the data

acquisition was performed at each 50 ps. As for interaction energy calculation, the time step was set as 1.0 fs and the COMPASS force field was used with the Berendsen algorithm to maintain a constant temperature (298 K) and pressure (100 kPa). Energy minimization method was employed to optimize the atomistic structures for 15000 steps so as to eliminate the local nonequilibrium, and then 150 ps NPT-MD runs were carried out to further equilibrate the models.

Corresponding formula

TOF measurements

The formula of turnover frequencies for all samples can be calculated as following:

$$\mathrm{TOF}(s^{-1}) = \frac{PV}{RT} \times COvol\% \times conversion\% / \frac{m}{M} / t$$

where P is the pressure (Pa), V is the volume of reactant gases through the reactor every minute (mL), R is the gas constant, and T is the room temperature (K), m is mass of total catalyst (g) and M is the molar mass (g/mol).

The specific reaction rate K can be calculated assuming the ideal gas behaviour as follows:

$$K\ (\mathrm{mol\ g^{-1}\ s^{-1}}) = \mathrm{GHSV\ (mL\ h^{-1}\ g^{-1})} \times 1/3600\ (\mathrm{h\ s^{-1}}) \times 1/1000\ (\mathrm{L\ mL^{-1}}) \times \mathrm{CO\ vol.\%} \times \mathrm{conversion\%} \times 1/22.4\ (\mathrm{mol\ L^{-1}}) \quad (1)$$

The specific reaction rate could be expressed by the Arrhenius equation:

$$K = A \exp(-E_a/RT) \quad (2)$$

where K is the reaction rate of CO (mol CO g^{-1} s^{-1}), A is the pre-exponential factor

(s^{-1}), Ea is the apparent activation energy (kJ mol^{-1}), R is the gas constant, and T is the absolute temperature (K). Taking the natural log of both sides of the equation (2), we get:

$$\ln K = -E_a/T + \ln A \quad (3)$$

By plotting ln K versus 1000/T, the apparent activation energy E_a can be calculated from the slope as shown in Figure S8.

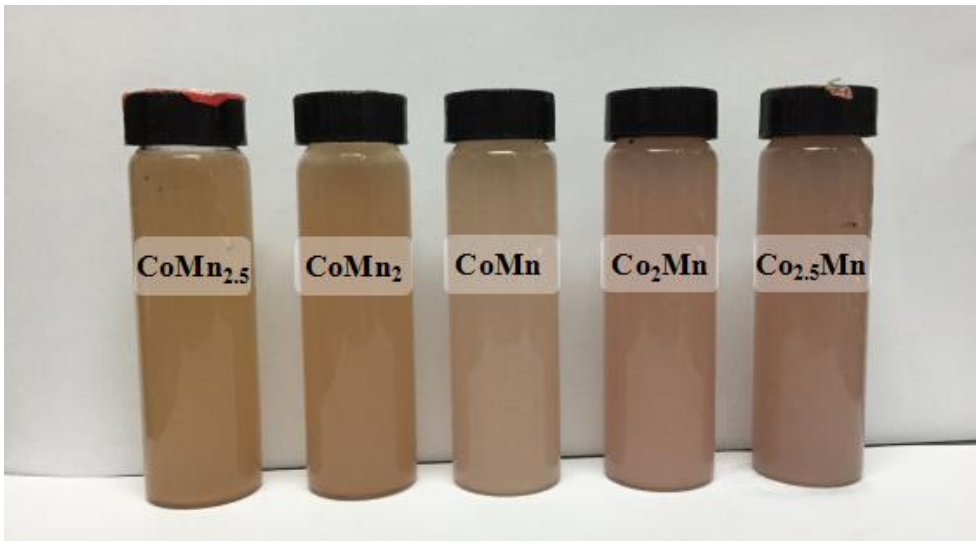

Figure S1. Photos of five different glycerate-CoMn precursors solutions after solvothermal treatment. The color of glycerate-CoMn precursor solutions presented deep organge yellow at high Mn loading. When the content of Co increased, the color of solutions changed from deep organge yellow to light pink. The color change of solution after solvothermal treatment indicated that the phase transformed through controlling the metal concentration. Related to Figure 1.

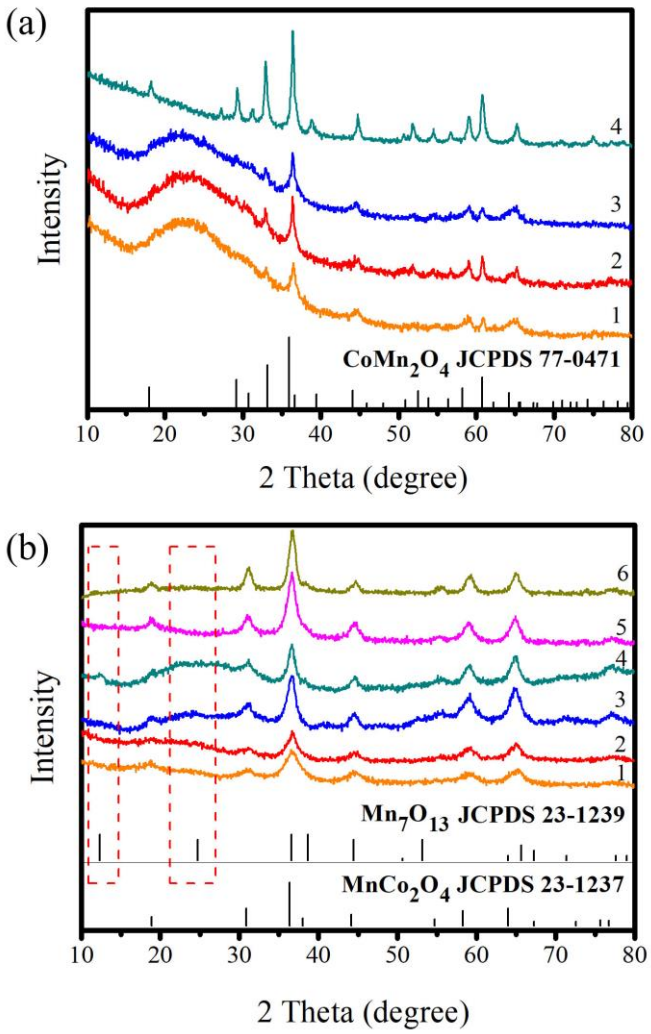

Figure S2. XRD patterns for characterizing intermediate. (**a**) Ex-situ XRD patterns of $CoMn_2$-glycerine after different heat treatment process:(1) calcined in air at 500 ^{o}C for 1 minute; (2) calcined in air at 500 ^{o}C for 15 minutes; (3) calcined in air at 500 ^{o}C for 30 minutes; (4) calcined in air at 500 ^{o}C for 2 h. (**b**) Ex-situ XRD patterns of Co_2Mn-glycerine after different heat treatment process: (1) calcined in air at 300 ^{o}C for 1 minute; (2) calcined in air at 400 ^{o}C for 1 minute; (3) calcined in air at 500 ^{o}C for 1 minute; (4) calcined in air at 500 ^{o}C for 15 minutes; (5) calcined in air at 500 ^{o}C for 30 minutes; (6) calcined in air at 500 ^{o}C for 2 h. Related to Figure 1.

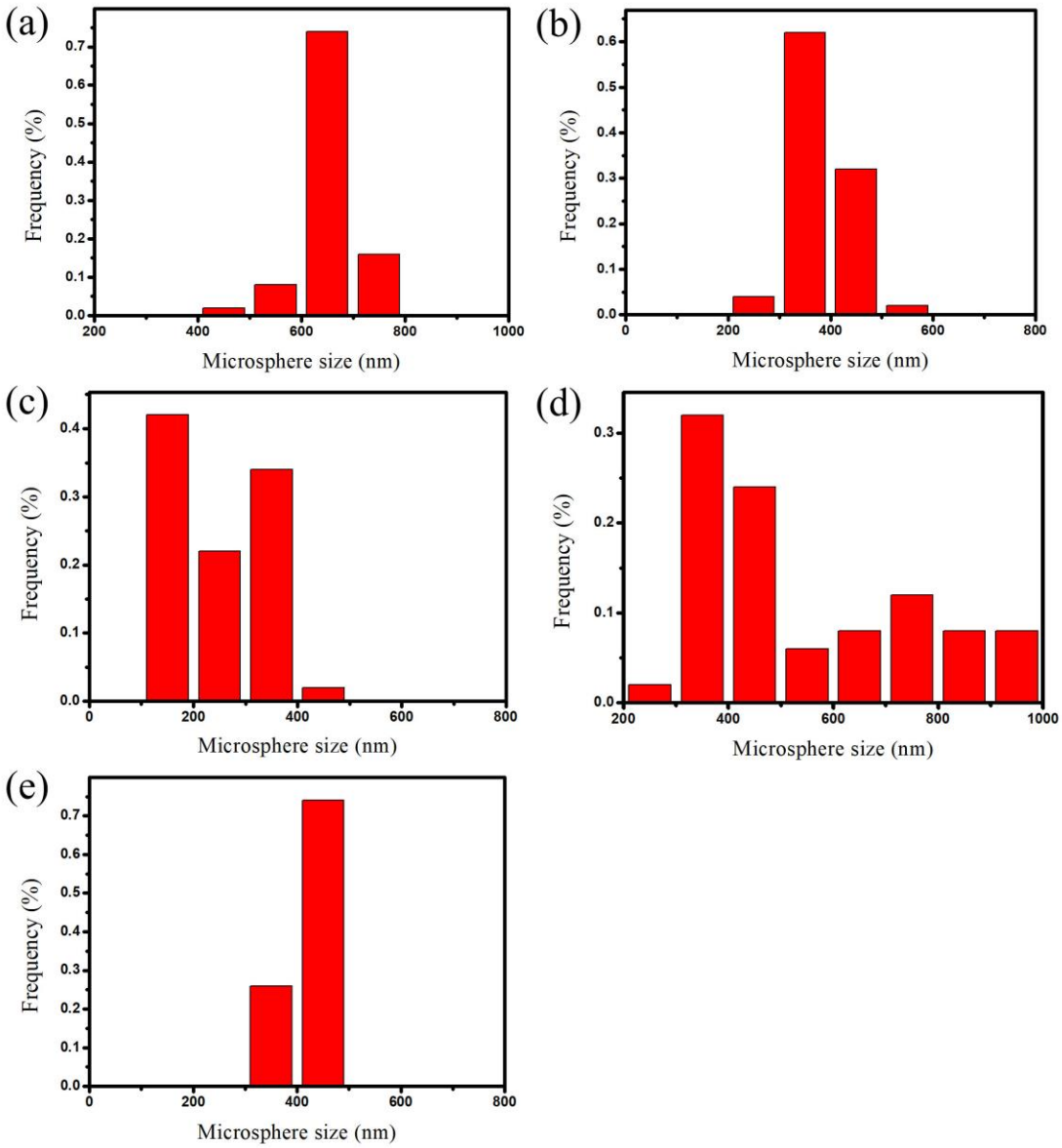

Figure S3. Microsphere size analysis. Size distribution of $CoMn_{2.5}O$-T (**a**), $CoMn_2O$-T (**b**), CoMnO-C (**c**), Co_2MnO-C (**d**) and $Co_{2.5}MnO$-C (**e**) spinels microspheres. The statistical data are based on the SEM images in Fig. 2. Related to Figure 2.

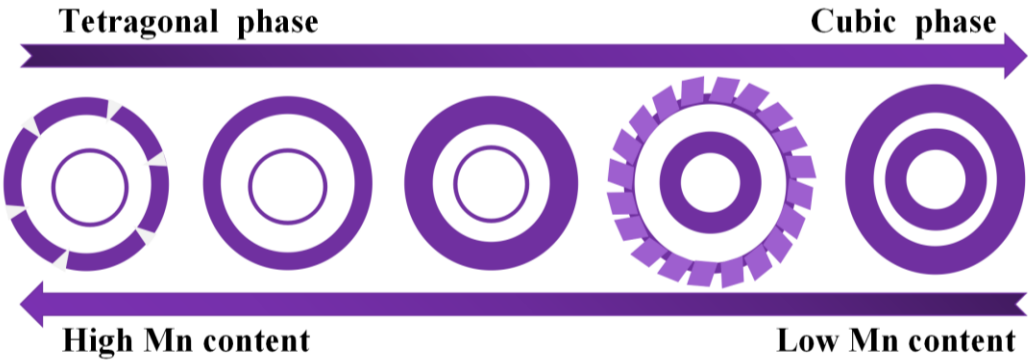

Figure S4. Schematic illustration of the formation process of prepared $Co_xMn_yO_4$ spinel hollow microspheres with phase transformation. At high Mn loading, the nanoparticles were randomly stacked on the surface to form thin shell with large pores. As the content of Mn decreased, the shell gradually became thick with the phase transformation from tetragonal from to cubic phase. Obviously, the flower-like Co_2MnO-C hollow microspheres can be generated by adjusting the loading of Co and Mn content. Related to Figure 1 and Figure 2.

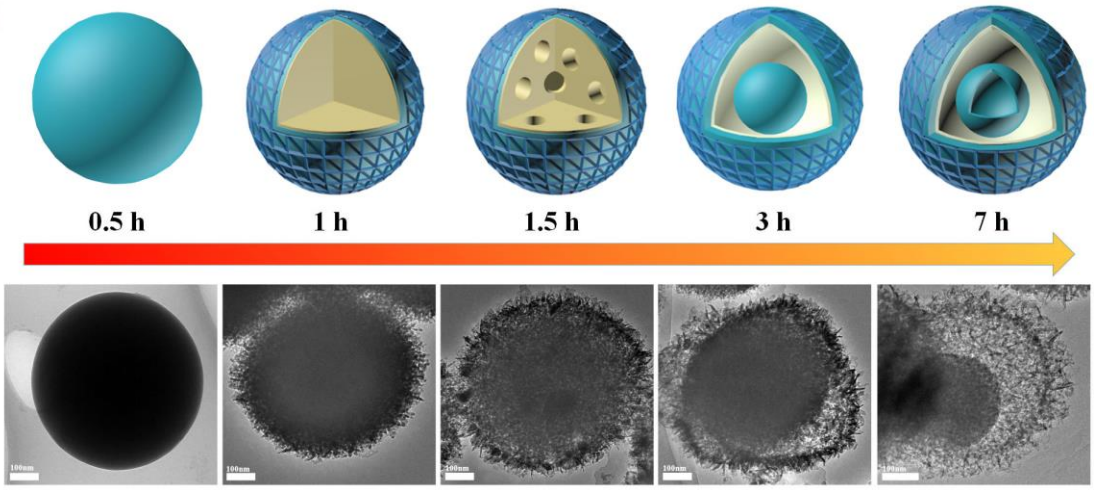

Figure S5. Schematic illustration of the formation process of Co_2MnO-C multishelled hollow microspheres and corresponding TEM images. When the reaction time reached 0.5 h, the low bet surface area (4.3 m^2/g) was confirmed by the nitrogen adsorption/desorption measurements (Fig. 3a and 3b). After subsequent 0.5 h solvothermal treatment, the surface of microspheres became rougher due to the generation of some small unordered nanoparticles on the surface. When the reaction time went up to 1.5 h, the whole precursor solid microsphere was disintegrated into a series of small nanoparticles, such a loose spongy structure in the interior of microsphere induced the generation of a number of small mesopores. Related to Figure 2.

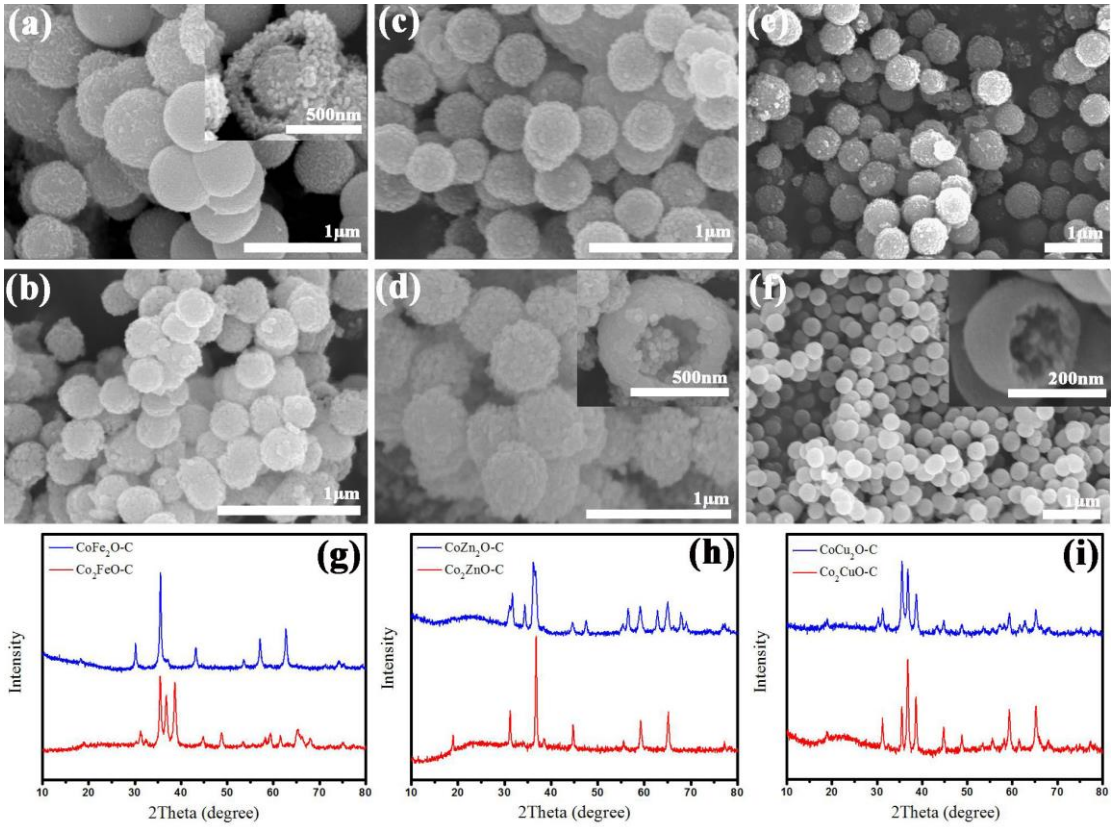

Figure S6. SEM images of substituted spinel microspheres. SEM images of $CoFe_2O$-C (**a**), Co_2FeO-C (**b**), $CoZn_2O$-C (**c**), Co_2ZnO-C (**d**), $CoCu_2O$-C (**e**) and Co_2CuO-C (**f**) hollow microspheres, the inset graphs are corresponding SEM images. XRD patterns of $Co_xFe_yO_4$-C (**g**), $Co_xZn_yO_4$-C (**h**) and $Co_xCu_yO_4$-C (**i**) hollow microspheres. The complex hollow microspheres have similar morphology and possess multi-shelled structure as $Co_xMn_yO_4$ spinel hollow microspheres. These bimetallic products are appreciated as solid catalysts, energy storage materials, magnetism, sensors and electronics. Related to Figure 3.

Table S1 Surface area and textural data for synthesized different samples.`

Sample	S_{BET} (m^2/g)[a]	BJH Average pore diameter (nm)[c]
Co_2MnO-C-0.5	4.3	3.69
Co_2MnO-C-1	22.9	2.55
Co_2MnO-C-1.5	48.2	2.54
Co_2MnO-C-3	127.5	3.18
Co_2MnO-C-7	203.5	3.59
$CoMn_2O$-T	81.9	6.15
$CoFe_2O$-C	89.1	13.05
Co_2ZnO-C	17.9	1.92
Co_2CuO-C	84.8	9.75

The specific surface areas of different kinds of microspheres are list in Table S1. The measured BET surface area of $CoMn_2O$-T sample showed a value of 81.9 m^2/g. It is worthy to note that the surface area of Co_2MnO-C sample reached the highest value of 203.5 m^2/g, which was due to the generation of numerous formed mesopores. However, the surface area of other multi-component metal oxide microspheres such as $CoFe_2O$-C, Co_2ZnO-C and Co_2CuO-C exhibited relatively lower surface area than that of Co_2MnO-C sample. Moreover, pore diameters were built up from 1.92 to 13.05 nm with the change of morphology. The results demonstrate that the bet surface areas and pore diameters can be tuned by changing the composition of microspheres. The formed mesoporous structure can greatly increase the mass transfer and lead to much better catalytic efficiency (Karger et al. 2013). Related to Figure 3 and Figure S5.

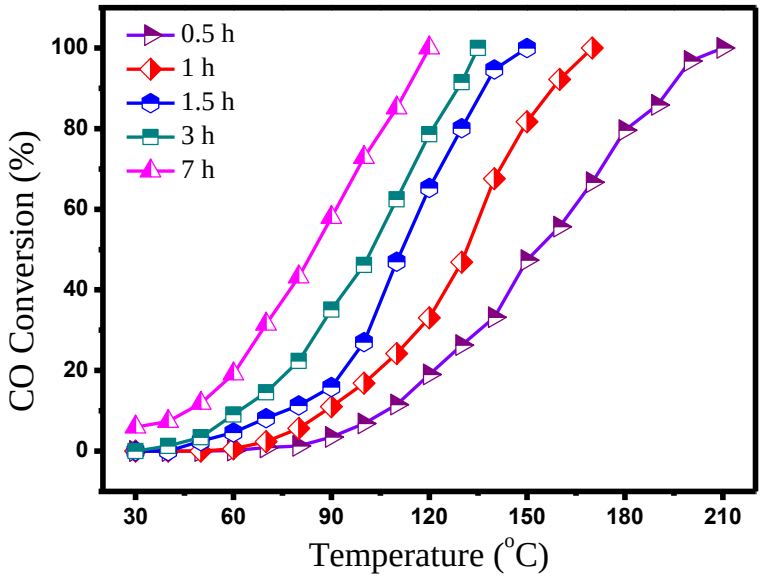

Figure S7. CO oxidation of Co_2MnO-C microspheres with different interior structure. Accordding to Figure S5, when the reaction time of synthetic procedure was 30 min, Co_2MnO-C microsphere exhibited low catalytic activity toward CO oxidation. By further enhancing the reaction time, the CO conversion gradually increased. This was attributed to the enlarged surface areas which provided more exposed active sites and weakened Co−O bond strength (Luo et al. 2008). Related to Figure 3.

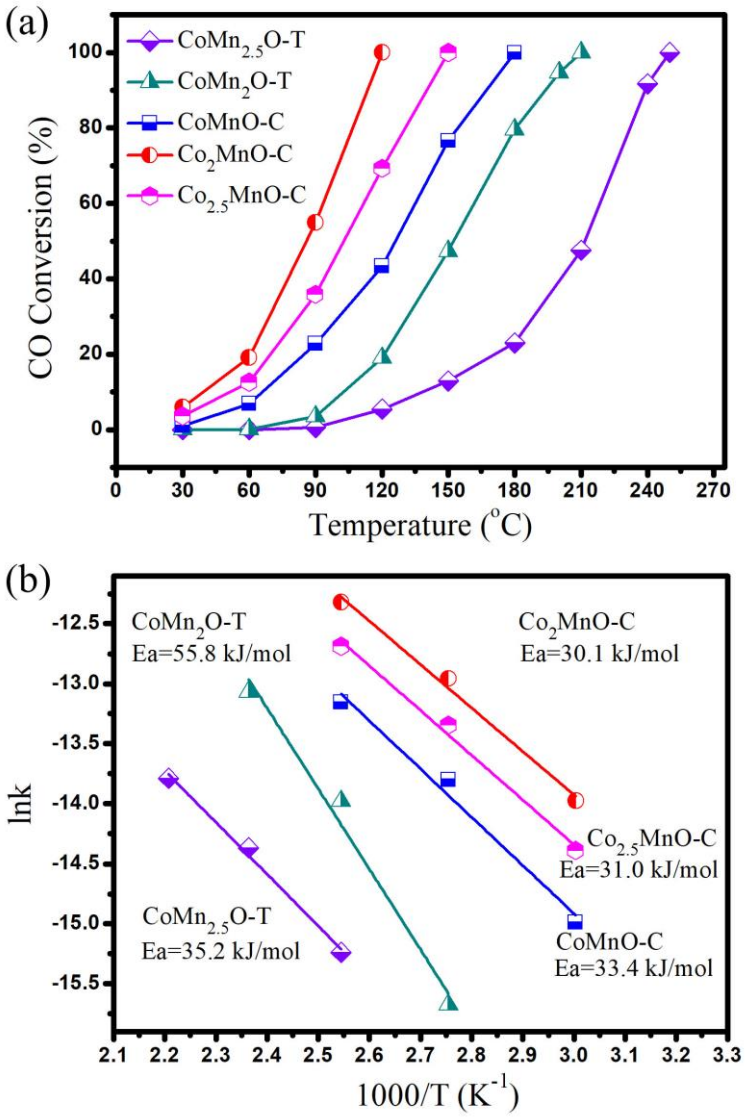

Figure S8. CO oxidation reaction measurements. (a) CO conversion as a function of reaction temperature for different $Co_xMn_yO_4$ spinel hollow microsphere catalysts. (**b)** The corresponding Arrhenius plots for the reaction kinetics. Related to Figure 3.

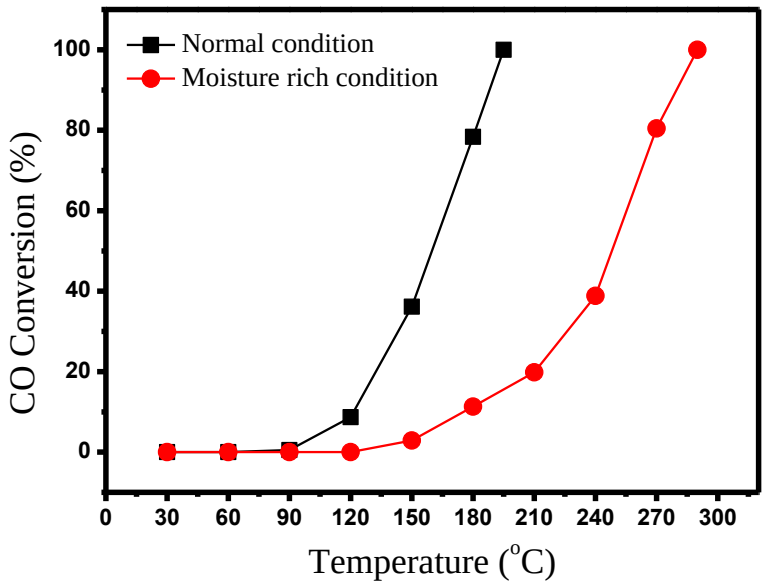

Figure S9. CO oxidation of hierarchical Co_3O_4 microsphere catalyst under normal and moisture rich conditions. Water-induced deactivation of the oxides catalysts still remains a big problem, especially for cobalt-based catalysts. H_2O dissociative adsorption happened in the oxygen vacancies and Co^{3+}, resulting the formation of carbonates (Shen et al. 2017). As predicted, the existence of H_2O in feed gas lowered the conversion of CO for Co_3O_4 microsphere catalyst. Related to Figure 3.

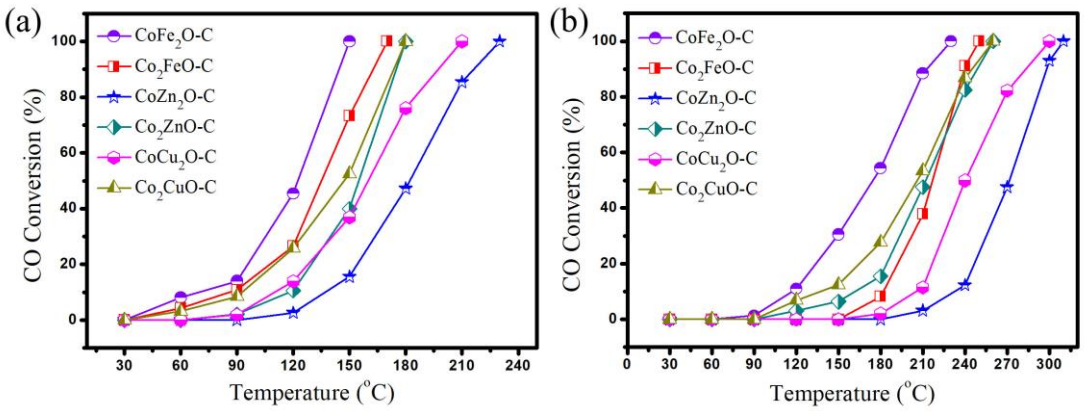

Figure S10. CO conversion as a function of reaction temperature for $Co_xFe_yO_4$-C, $Co_xZn_yO_4$-C and $Co_xCu_yO_4$-C samples under normal conditions (a) and moisture rich conditions (~2% H_2O) (b). The prepared bimetallic spinel multishelled hollow microspheres ($Co_xFe_yO_4$, $Co_xZn_yO_4$ and $Co_xCu_yO_4$) showed weak water-resisting property compared with cobalt manganese spinel samples. Related to Figure 3.

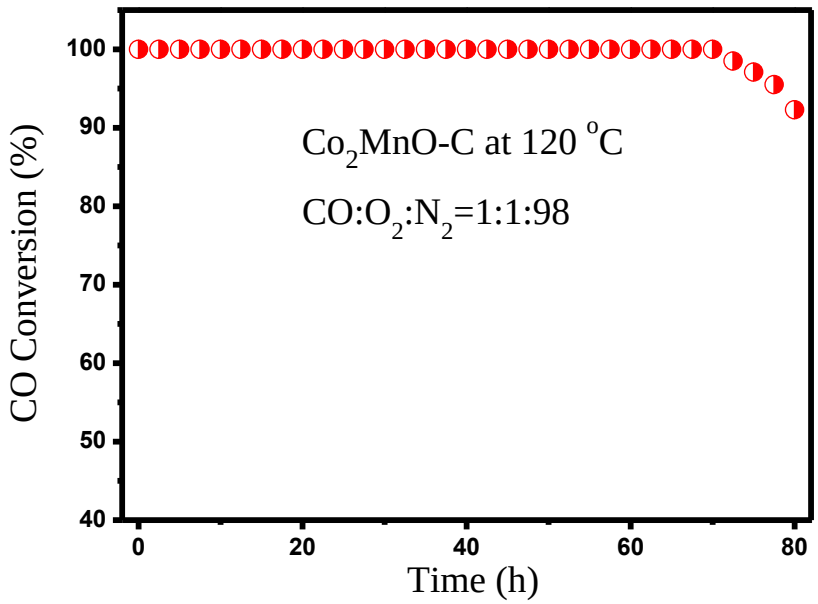

Figure S11. Stability test of Co_2MnO-C hollow microspheres under normal condition. The graph above displays the CO conversion of Co_2MnO-C hollow microsphere catalysts during 80 h reaction. As noticed, the Co_2MnO-C sample exhibited almost no decline in CO conversion before a long period of 71 h. Related to Figure 3.

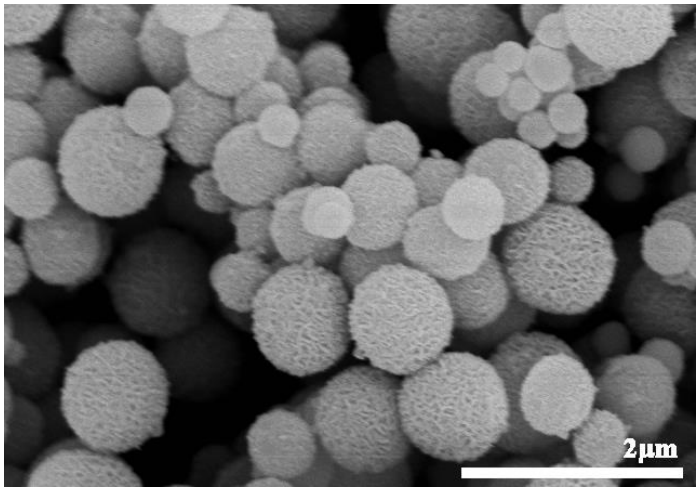

Figure S12. SEM images of Co_2MnO-C microspheres after multiple uses in catalysis. The prepared Co_2MnO-C microspheres kept the same morphologies after multiple uses. Related to Figure 3.

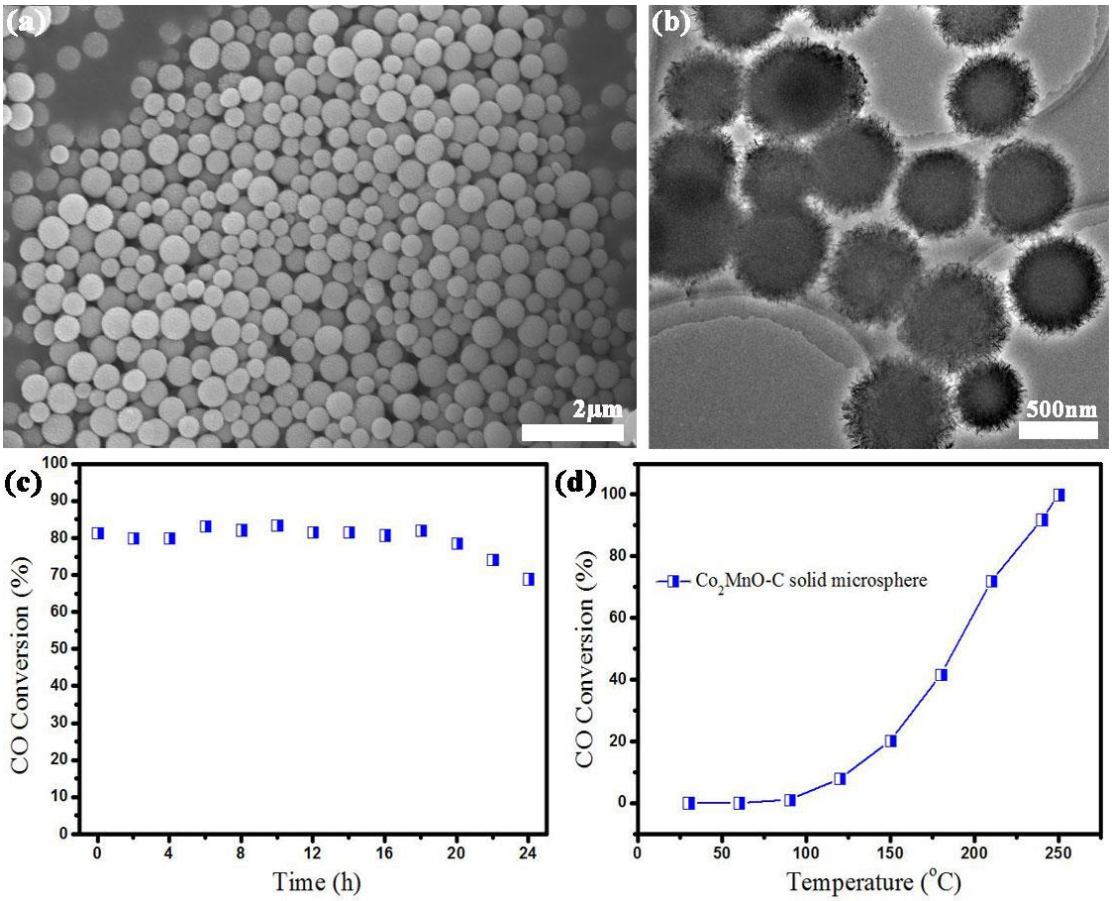

Figure S13. Morphology and catalytic performance of Co_2MnO-C solid microspheres. SEM (**a**) and TEM (**b**) images of Co_2MnO-C solid microspheres. (**c**) Stability test of of Co_2MnO-C solid microspheres at 150 ^oC under normal conditions. (**d**) Light-off curves for CO oxidation on Co_2MnO-C solid sample in the gas stream containing ~2% moisture. As predicted, the Co_2MnO-C solid sample showed low catalytic activity and stability compared with hollow Co_2MnO-C microspheres. Related to Figure 3.

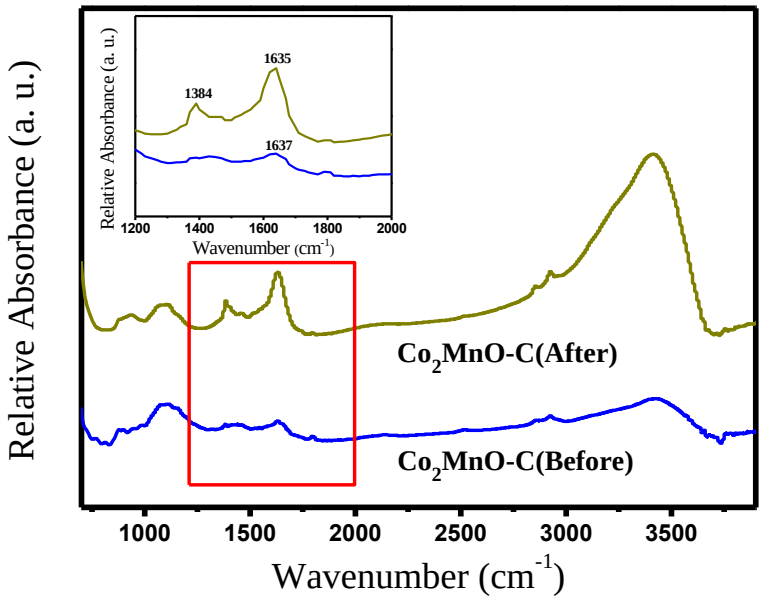

Figure S14. FTIR spectra of Co_2MnO-C hollow microspheres before and after stability tests under normal conditions. The bands around the 1637 cm^{-1} can be assigned to the vibration of adsorbed water. It is worthy to note that the new peaks (inserted graph) at 1384 cm^{-1} is due to the formation of formate or carbonate-like species (Poyraz et al. 2013), which induces the decrement of activity for Co_2MnO-C hollow microspheres. Related to Figure 3.

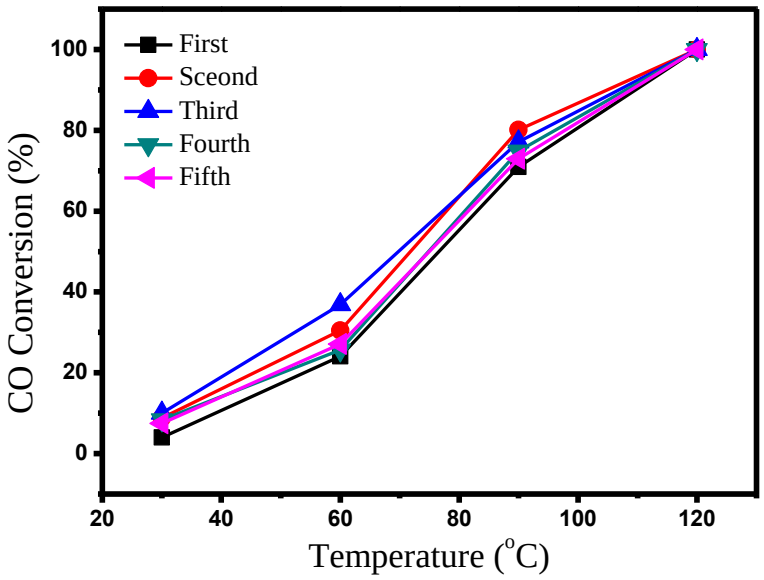

Figure S15. Reusability of catalysts after subsequent reactions. As cobalt-based species are usually unstable during reaction, it is necessary for practical applications to develop methods to regenerate these species. In this work, it was found that high-temperature calcination in air helped to restore catalytic activity. The CO oxidation curves of Co_2MnO-C sample show that excellent reusability of catalyst can be achieved just simply after 600 ^{o}C oxidation treatment. Related to Figure 3.

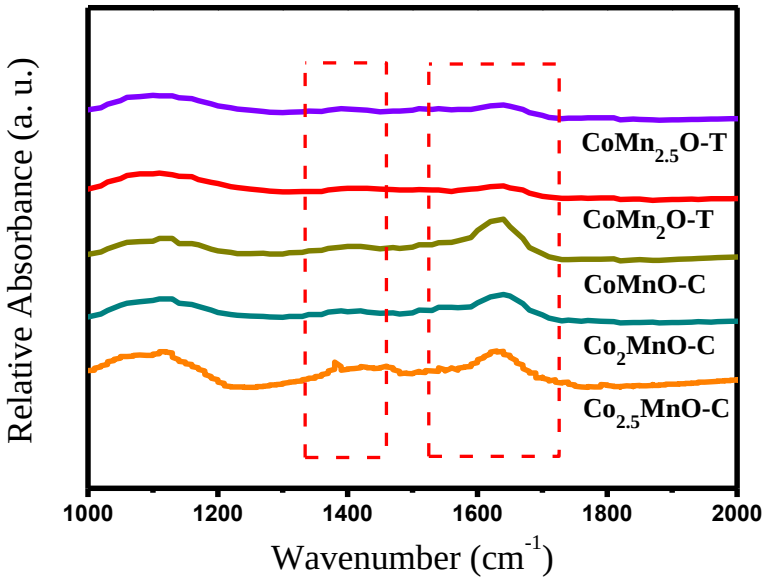

Figure S16. FTIR spectra of five different cobalt manganese spinel hollow microsphere catalysts after stability tests under moisture conditions for 2 h. The bands around 1635 cm^{-1} are attributed to the vibration of adsorbed water molecular (19). The results reveal that the amounts of adsorbed water on the surface of prepared spinel samples were sharply reduced in Mn rich environment. Interestingly, bits of adsorbed H_2O reversed carbonate species formation and prevented the deactivation of as-synthesized catalysts during further operation. Related to Figure 3.

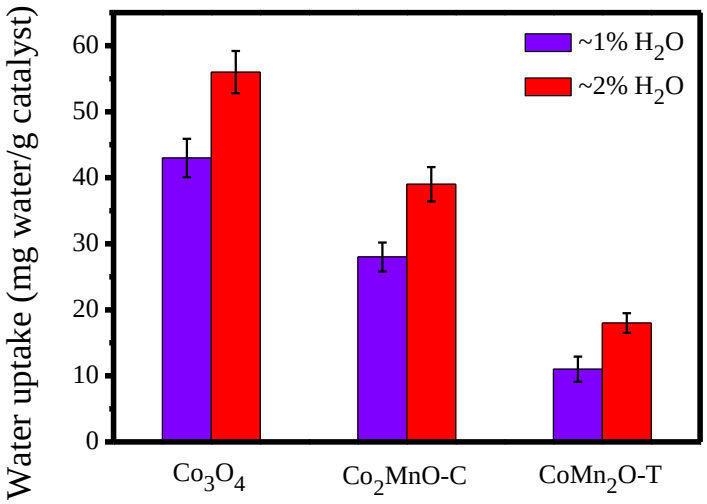

Figure S17 Water adsorption of pure Co_3O_4 hollow microsphere, Co_2MnO-C and $CoMn_2O$-T samples at different moisture conditions for 3 h. The introduction of Mn into hollow microsphere obviously reduced the water uptake amount. The water uptake amount of $CoMn_2O$-T sample was 4 and 3 times lower than that for the pure Co_3O_4 hollow microsphere under ~1% H_2O and ~2% H_2O condition, respectively. Related to Figure 3.

Table S2 Comparison of CO total conversion under normal and moisture rich conditions with references (T_1- Total conversion under normal conditions, T_2- Total conversion under moisture rich conditions, ΔT-Difference between T_1 and T_2).

Samples	T_1	T_2	ΔT	Morphology	TOF (s^{-1}) at 80 °C	Ref
Co_3O_4@ CNT	25 °C	175 °C (~3% H_2O)	150 °C	Nanoparticles	2.41×10^{-5}	Kuo et al. 2014
F−Co_3O_4@ CNT	25 °C	150 °C (~3% H_2O)	125 °C		9.68×10^{-5}	
Co_3O_4	-78 °C	100 °C (0.6 vol % H_2O)	178 °C	Nanoparticles	3.31×10^{-5}	Shen et al. 2017
$Fe_3Co_{16}O_x$	-96 °C	70 °C (0.6 vol % H_2O)	166 °C		7.17×10^{-5}	
$Mn_{0.75}Co_{2.25}O_4$	20 °C	90 °C (0.45 vol % H_2O)	70 °C	Nanoparticles	6.30×10^{-5}	Wang et al. 2014
Co_3O_4	-80 °C	20 °C (13840-15780 ppm H_2O)	100 °C	Nanoparticles	/	Yu et al. 2009
$Cu_{1.5}Mn_{1.5}O_4$	150 °C	300 °C (1.7 vol % H_2O)	150 °C	Nanoparticles	/	Biemelt et al. 2016
Cu-CeO_2	60 °C	130 °C (~0.03% H_2O)	70 °C	Nanoparticles	2.72×10^{-5}	Zhang et al. 2005
Ag/Fe_2O_3	325 °C	425 °C (~20% H_2O)	100 °C	Nanoparticles	9.63×10^{-5} (150 °C)	Biabani-Ravandi et al. 2013
Co_2MnO-C	170 °C	250 °C (~2% water vapor)	80 °C	Solid sphere	4.86×10^{-6}	This work
$CoMn_{2.5}$O-T	250 °C	270 °C (~2% water vapor)	20 °C	Double-shelld hollow sphere	9.45×10^{-5}	
$CoMn_2$O-T	210 °C	250 °C (~2% water vapor)	40 °C		1.89×10^{-6}	
CoMnO-C	180 °C	220 °C (~2% water vapor)	40 °C		4.97×10^{-5}	
Co_2MnO-C	120 °C	170 °C (~2% water vapor)	50 °C		1.75×10^{-4}	
$Co_{2.5}$MnO-C	150 °C	200 °C (~2% water vapor)	50 °C		7.72×10^{-5}	

Related to Figure 3.

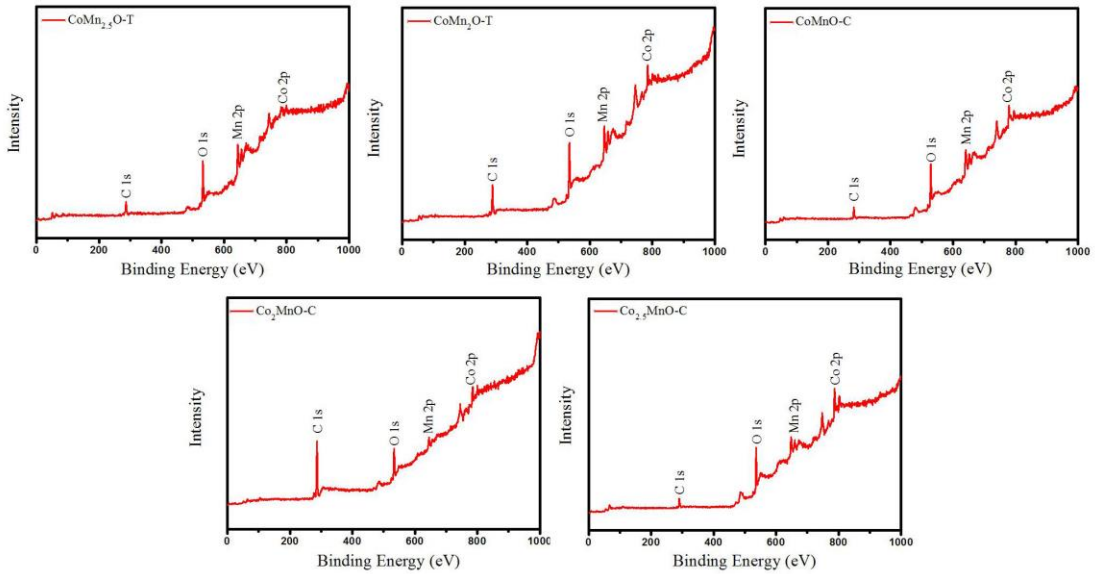

Figure S18. XPS full spectra of five kinds of cobalt manganese spinel hollow microspheres. The full spectra reveal the presence of the C, O, Mn and Co elements. No impurities are observed in the samples. Related to Figure 4.

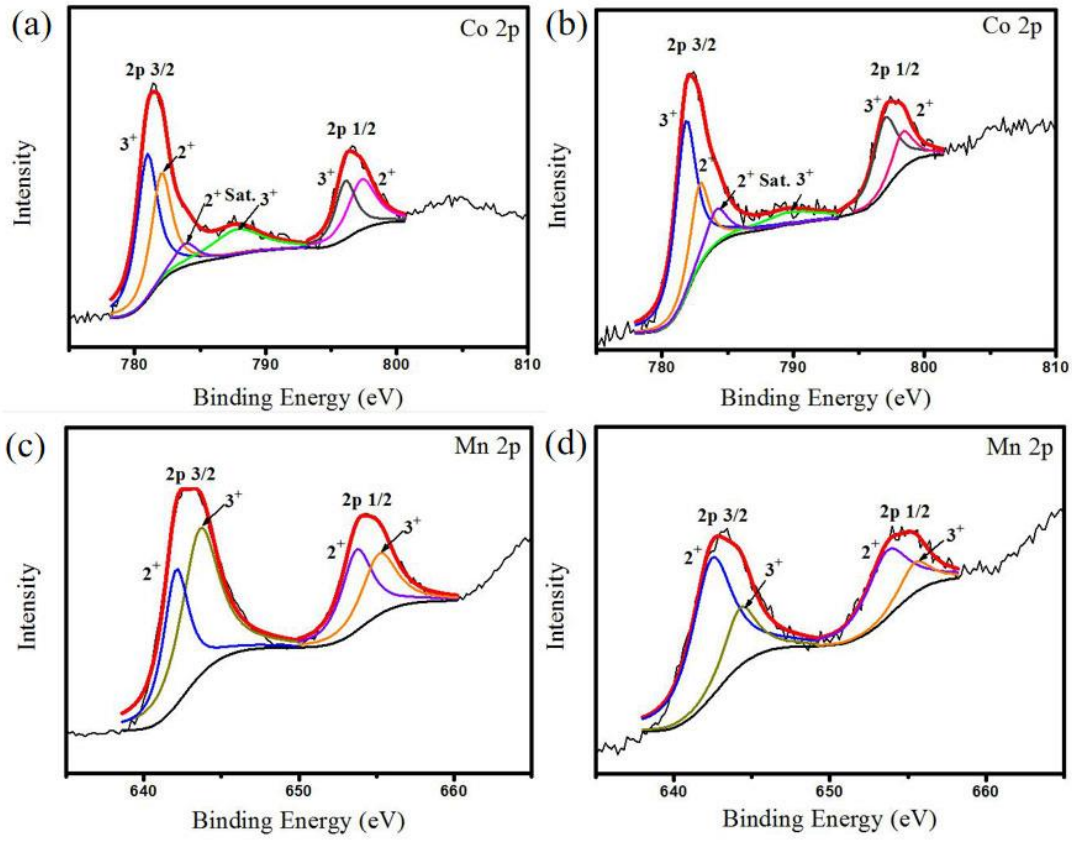

Figure S19. XPS spectra spectra of $CoMn_2O$-T (a, c), Co_2MnO-C (b, d) samples. The Co 2p spectra are best fitted into two spin-orbit doublets characteristic of Co^{2+} and Co^{3+} and one shake-up satellites through adopting Gaussian fitting method. The observation of the satellite peak near 788 eV in graphs suggests the presence of Co^{3+}. The Mn 2p spectrum is also achieved under the assumption of two pairs of spin-orbit doublets, the spectrum can be divided into four distinct peaks after refined fitting. Among them, 641.6 and 653.1 eV are ascribed to the existence of Mn^{2+}, and other two peaks located at 642.6 and 654.0 eV can be specified to trivalent manganese ion. Related to Figure 4.

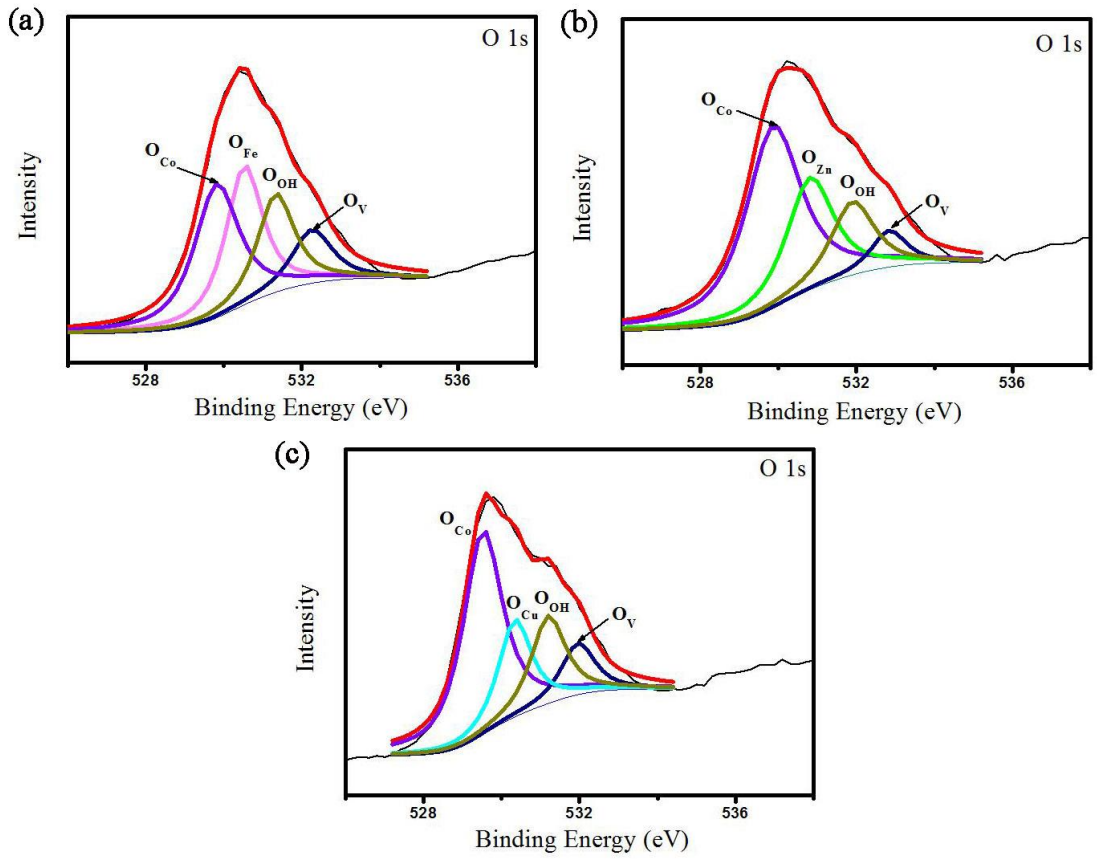

Figure S20. XPS spectra of O 1s peaks for $CoFe_2O$-C (a), Co_2ZnO-C (b) and Co_2CuO-C (c) spinel hollow microspheres. The fitted O 1s spectra display four major oxygen contributions with the corresponding peaks centered at ~529, 530, 531, and 532 eV, respectively. These bands can be attributed to Co-O bonds (O_{Co}), M-O (M=Fe, Zn and Cu) bonds (O_M), hydroxyl (O_{OH}), oxygen vacancies (O_v). Related to Figure 4.

Table S3 The area percentages of O elemental components calculated from the XPS spectra.

	O 1s						
sample	O_{Co} (%)	O_{Mn} (%)	O_{Fe} (%)	O_{Zn} (%)	O_{Cu} (%)	O_{OH} (%)	O_V (%)
$CoMn_{2.5}O$-T	23.22	44.95	/	/	/	25.16	6.67
$CoMn_2O$-T	30.02	40.61	/	/	/	20.12	9.25
CoMnO-C	37.93	31.82	/	/	/	18.53	11.71
Co_2MnO-C	36.75	25.74	/	/	/	22.77	14.72
$Co_{2.5}MnO$-C	48.36	18.03	/	/	/	21.45	12.16
$CoFe_2O$-C	30.27	/	35.39	/	/	21.55	12.78
Co_2ZnO-C	50.97	/	/	26.52	/	15.97	6.53
Co_2CuO-C	50.41	/	/	/	20.08	18.70	10.79

Related to Figure 4.

Table S4 The area percentages of O elemental components calculated from the APXPS spectra.

	O 1s			
Sample	O_{Co} (%)	O_{Mn} (%)	O_{OH} (%)	O_V (%)
$CoMn_{2.5}O$-T	25.03	51.39	17.26	6.32
$CoMn_2O$-T	30.22	41.10	20.10	8.58
CoMnO-C	35.71	32.55	20.38	11.36
Co_2MnO-C	40.02	23.94	22.69	14.35
$Co_{2.5}MnO$-C	46.17	25.18	15.92	11.73

Related to Figure 4.

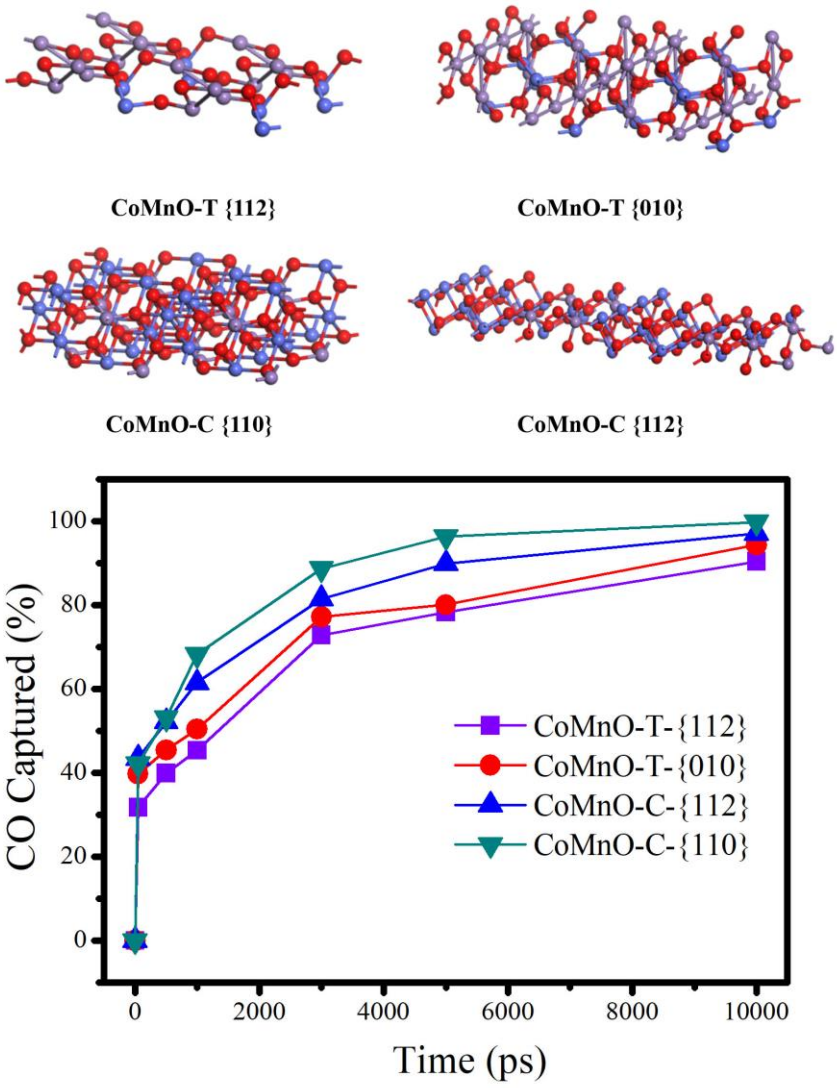

Figure S21. Molecular dynamics simulations. The percentage of CO adsorbed on four kinds of planes of cobalt manganese spinels for 10 ns. Related to Figure 4.

Table S5 Calculated interaction energies of between gas molecules and cobalt manganese spinel exposed different facets.

Sample	Interaction energy toward CO (kcal/mol)	Interaction energy toward CO_2 (kcal/mol)
CoMnO-T-{112}	-3.47±0.25	-0.73±0.11
CoMnO-T-{010}	-3.62±0.36	-0.43±0.08
CoMnO-C-{110}	-4.66±0.31	-0.31±0.05
CoMnO-C-{112}	-4.12±0.29	-0.35±0.05

After the optimization of the tetragonal phase {010} and {112} surface and cubic phase {110} and {112} surface, we studied their interactions with the molecules in this investigation. The electrostatic interaction energy between gas molecules (CO or CO_2) and cobalt manganese spinel exposed different facets was defined as:

$$E=E_{CoMnO\text{-}\{hkl\}+gas} -(E_{CoMnO\text{-}\{hkl\}} + E_{gas})$$

where $E_{CoMnO\text{-}\{hkl\}+gas}$ is the total energy of gas molecules and cobalt manganese spinel exposed different facets; $E_{CoMnO\text{-}\{hkl\}}$ and E_{gas} are total energy of cobalt manganese spinel exposed different facets and gas molecules (CO or CO_2), respectively. Related to Figure 4.

Supplementary references

Biabani-Ravandi, A., Rezaei, M., Fattah, Z. (2013). Catalytic performance of Ag/Fe_2O_3 for the low temperature oxidation of carbon monoxide. Chem. Eng. J. 219, 124-130.

Karger, J., Valiullin, R. (2013). Mass transfer in mesoporous materials: the benefit of microscopic diffusion measurement. Chem. Soc. Rev. 42, 4172-4197.

Luo, J., Meng, M., Li, X., Li, X. G., Zha, Y., Hu, T., Xie, Y., Zhang, J. (2008). Mesoporous Co_3O_4-CeO_2 and Pd/Co_3O_4-CeO_2 catalysts: Synthesis, characterization and mechanistic study of their catalytic properties for low-temperature CO oxidation. J. Catal. 254, 310-324.

Poyraz, A. S., Kuo, C.-H., Biswas, S., King'ondu, C. K., Suib, S. L. (2013). A general approach to crystalline and monomodal pore size mesoporous materials. Nat. Commun. 4, 2952.

Shen, Y., Yu, J., Xiao, X., Guo, X., Mao, D., Huang, H., Lu, G. (2017). Polymer nanofilm-coated catalysis: An approach for enhancing waterresistance of Co-Fe oxide nano-catalysts under moisture-rich condition. J. Catal. 352, 466-479.

Wang, Q., Duan, W. H., Richards, N. L., Liew, K. M. (2007). Modeling of fracture of carbon nanotubes with vacancy defect. Phys. Rev. B 75, 239901.

Zhang, W., PalDey, S., Deevi, S. (2005). Effect of moisture on the active species in Cu-CeO_2 catalyst. Appl. Catal., A 295, 201-208.